CFD Modeling of Binary-Fluidized Suspensions and Investigation of Role of Particle–Particle Drag on Mixing and Segregation

Olumuyiwa Owoyemi, Luca Mazzei, and Paola Lettieri
Dept. of Chemical Engineering, University College London, Torrington Place, London, WC1E 7JE, U.K.

DOI 10.1002/aic.11227

A model is presented for the prediction of the fluid dynamic behaviour of binary suspensions of solid particles fluidized by Newtonian fluids. The equations of motion for the fluid and solid phases are derived by extending the averaged two-fluid equations of change for identical spheres in Newtonian fluids developed by Anderson and Jackson and Jackson. A new closure relationship for the fluid–particle interaction force is employed and a new numerical algorithm is developed to control the solid compaction in each particle phase. The article also presents a comparison between three different equations of closure for the particle–particle drag implemented within the model. Predictions of the fluidization behavior obtained by the proposed model are validated against experimental results in terms of solid mixing and segregation, bed expansion and bubble dynamics. Two-dimensional CFD simulations are performed in a bed of rectangular geometry using ballotini with particle sizes of 200 and 350 μm.
AIChE J, 53: 1924–1940, 2007
Keywords: fluidization, multiphase flow, CFD, binary systems, equations of change, particle–particle drag, mixing and segregation, bubble dynamics

Introduction

The availability of advanced commercial computational fluid dynamics (CFD) software and of faster computer processors have revolutionized scientific research in the field of multiphase flow. CFD has become an indispensable tool, for researchers and engineers alike, in solving many complex problems of academic and industrial interest in areas such as fluidization, combustion, oil flow assurance as well as aerospace science. In the field of fluidization, in particular, the use of CFD has pushed the frontier of fundamental understanding of fluid–solid interactions and has enabled the correct theoretical prediction of various macroscopic phenomena encountered in fluidized beds. Indeed many CFD simulations of monocomponent fluidized systems have been carried out by researchers covering the whole range of Geldart classified powders with great success.[1–5] More recently, the simulation of industrial monosize powders has also been successfully tackled by Owoyemi et al.[6] using a Eulerian–Eulerian approach. The various two-fluid models employed by the above-named authors have common origins in the spatially averaged Eulerian–Eulerian equations of motion first put forward by Anderson and Jackson[7] and successively rigorously derived by several other researchers.[8–14] Such equations, as it is well known, are not mathematically closed and necessitate

---

Correspondence concerning this article should be addressed to Paola Lettieri at p.lettieri@ucl.ac.uk.

empirical closures for contributions mainly related to the internal stress associated to each phase and to the fluid–particle interaction force. The need for suitable closures, indispensable for predicting the dynamics of multiphase systems with a satisfactory degree of accuracy, has stimulated a vast amount of original research that has led to the pervasiveness of many empirical closures in literature today.

A monosize system of particles seldom occurs in a fluidized bed of practical importance. Industrially operated fluidized beds typically consist of particles, which have a wide size distribution as well as different densities. The phenomenon of mixing and segregation becomes of major importance in these nonideal systems. A vast amount of experimental work has already been carried out by many authors looking at the behavior of binary mixtures in gas-fluidized beds and in particular at the segregation rate, which they display.[15–18] The rate of segregation is often measured using the bed freeze test, where particles are taken from the fluidized bed layer by layer and sieved separately to measure the concentrations of different species.[19] The computational modeling of binary systems, conversely, has not met with the same resounding success. The continuum modeling of binary mixtures is typically carried out using two approaches. The first is characterized by the use of separate momentum equations to cater for each particle species, whilst the second makes use of averaged mixture properties for the formulation of a mixture momentum equation coupled with the use of averaged constitutive relations.

Each of the two modeling approaches described above has been applied separately to simulate particulate flow patterns within gas-fluidized beds. The first approach based on separate momentum equations has been employed by a few authors.[20–23] Their investigations, carried out using Geldart Group D particles, report good model predictions with a limited set of experimental measurements. The second approach based on the mixture momentum balance has been employed by van Wachem et al.[24] to predict the flow of a binary-fluidized suspension of Geldart Group B particles. Results from the work showed good predictions with regard to bed expansion and minimum fluidization velocity.

The relatively little research conducted in the field of CFD involving binary mixtures and more generally mixtures with a particle size distribution (PSD) does not yet allow accurate theoretical predictions of the flow behavior of such systems. The work presented in this article is primarily concerned with the modeling of noncohesive binary-fluidized suspensions of solid particles; the approach adopted is that based on separate equations of motion as opposed to the mixture approach previously described. The authors propose to address some conceptual questions that naturally arise when modeling binary mixtures and which relate, for instance, to the nature of the particle–particle drag and of the internal stress associated to each phase.

The use of separate momentum equations for each particulate phase in the modeling of binary mixtures requires an extra term to account for the collisions between particles that belong to different size classes. This extra contribution should be termed *particle–particle interaction force*, but is often referred to as *particle–particle drag force*. Indeed, strictly speaking, the two forces are not equivalent, since the former might encompass several contributions, of which the drag is just one. The earliest attempt to quantify the nature of this force was made by Soo[25] where a derivation was given for the force acting on a single particle of species F_1 in a cloud of colliding particles of species F_2. This was followed by a similar development by Nakamura and Capes.[26] An experimentally related theoretical development was carried out by Arastoopour et al.,[27] where a semiempirical expression was derived for dilute gas–solid systems. Several expressions have since been put forward by many authors[20–22,28,29] with most correlations being variations of earlier pioneering developments.

In the first section of this article, a derivation of the Eulerian–Eulerian averaged equations of motion for binary mixtures of particles in Newtonian fluids is presented. These equations are an extension of those originally put forward by Anderson and Jackson[7] and Jackson[8,9] for systems of monosize particles in Newtonian fluids, where the averaged equations of conservation for mass, linear and angular momentum were derived and phase interactions modeled phenomenologically. In our derivation, however, only the mass and linear momentum equations of conservation shall be considered. These suffice to provide a rich description of the fluid–solid interaction forces at play in binary mixtures and a logical justification for the emergence of terms such as the particle–particle interaction force or the stress tensors associated with each phase.

A brief description of a new fluid dynamic model developed by the authors for binary-fluidized mixtures and implemented in the commercial CFD code CFX 4.4 follows thereafter. In this model, the fluid dynamic interaction between fluid and solid is based on the "elastic force" concept originally proposed by Wallis.[30] The solid stress tensors are neglected, and a new numerical scheme is proposed to control the solid compaction in each particle phase.

A substantiation of the effect of the particle–particle drag force on the mixing and bubble dynamics of a binary gas–solid fluidized bed concludes the work. Here, three different closures available in literature and catering for this contribution are considered. The simulations are compared with a reference simulation where interphase particle–particle interactions are entirely neglected, and with dedicated experimental results. The particles used for experiments and computational studies belong to the Geldart Group B classification and are 200 and 350 μm in diameter respectively and have a density of 2500 kg/m^3.

Equations of Change for Binary Mixtures in Newtonian Fluids

In this section, we seek to derive the averaged equations of motion for binary mixtures to elucidate the origin of the internal stress, fluid–particle, and particle–particle interaction forces at play in such systems and provide a mathematical basis for these contributions. The formal process of local space averaging is used to obtain the macroscopic equations of conservation for binary systems from microscopic balance equations. This form of local averaging was first advanced by Anderson and Jackson[7] and has since been used by many authors, though in slightly different form. In this method, a weighting function is introduced to obtain the averaged values of point properties, which could be scalar, vectorial, or tensorial. The weighting function, in this instance, is used as a device to give "weight" to elements closer to the spatial position wherein the average is computed. The point variables are averaged over regions, which are large with respect to the particle diameter but small with respect to the macroscopic length scale of interest.

In what follows, we extend the original work by Jackson[8,9] by deriving new spatially averaged Eulerian–Eulerian equations of motion suitable for binary systems of solid particles fluidized by Newtonian fluids. We also propose a new contact force in the particle phase momentum equations that accounts for the force exerted by particles that belong to different solid phases at their mutual point of contact. In the mathematical derivation, the convention is adopted that repeated *lower* indices are summed over the values one to three; upper indices are *not* to be regarded as dummy indices implying summation. Two arbitrary size classes, F_1 and F_2, shall be considered, which are representative of the two different types of particles present in the mixture.

Averaged equations of motion for the fluid phase

By applying the averaging scheme described by Jackson[8,9] to a binary system, we now derive the locally averaged equations of conservation for mass and linear momentum for the fluid phase. To this end, the original averaging procedure must be slightly modified to suit the physical system at hand. Most of the modifications, however, are quite straightforward and shall be omitted for the sake of brevity; the mathematical passages shall be described in detail only when the derivation substantially differs from the original formulation.

In the assumption of incompressibility, the averaged continuity equation for the fluid phase takes the form:

$$\frac{\partial \varepsilon}{\partial t}+\frac{\partial}{\partial x_k}\left(\varepsilon\langle u_k\rangle^{\mathrm{f}}\right)=0 \qquad (1)$$

where $\varepsilon(\boldsymbol{x},t)$ is the fluid volume fraction and $\langle u_k\rangle^{\mathrm{f}}\ (\boldsymbol{x},t)$ is the kth component of the averaged fluid velocity. It is worth stressing that, as indicated, both variables are functions of spatial position and time; to simplify the mathematical notation, however, the dependence on either or both independent variables will be often left out.

The averaged dynamical equation for the continuous phase is obtained by averaging the fluid microscopic linear momentum equation of conservation; the resulting equation is:

$$\rho_{\mathrm{f}}\left[\frac{\partial}{\partial t}\left(\varepsilon\langle u_i\rangle^{\mathrm{f}}\right)+\frac{\partial}{\partial x_k}\left(\varepsilon\langle u_i\rangle^{\mathrm{f}}\ \langle u_k\rangle^{\mathrm{f}}\right)\right] = \frac{\partial\langle S\rangle_{ik}^{\mathrm{f}}}{\partial x_k}-n_1\langle f_i^{\mathrm{f}}\rangle^{\mathrm{F}_1}-n_2\langle f_i^{\mathrm{f}}\rangle^{\mathrm{F}_2}+\varepsilon\rho_{\mathrm{f}}g_i \qquad (2)$$

where ρ_{f} is the fluid density, $n_1(\boldsymbol{x},t)$ and $n_2(\boldsymbol{x},t)$ are the particle number densities (number of particles per unit volume) of phases F_1 and F_2, respectively, and g_i is the ith component of the gravitational acceleration. The terms $n_1\langle f_i^{\mathrm{f}}\rangle^{\mathrm{F}_1}\ (\boldsymbol{x},t)$ and $n_2\langle f_i^{\mathrm{f}}\rangle^{\mathrm{F}_2}\ (\boldsymbol{x},t)$, related to the fluid–particle interaction force, are given by the expression:

$$n_j\langle f_i^{\mathrm{f}}\rangle^{\mathrm{F}_j}(\boldsymbol{x},t)=\sum_{\mathrm{F}_j}\left\{g\left(\left|\boldsymbol{x}-\boldsymbol{x}^{c_j}\right|\right)\int_{S_j}\xi_{ir}(\boldsymbol{y})n_r(\boldsymbol{y})dS_y\right\};\qquad j=1,2 \qquad (3)$$

Here and in what follows, $g(|\boldsymbol{x}-\boldsymbol{y}|)$ denotes the weighting function used in the averaging procedure; the norm $|\boldsymbol{x}-\boldsymbol{y}|$ represents the separation of two points in space: $\boldsymbol{x}$ being the spatial point in which the average is worked out and $\boldsymbol{y}$ being a mute variable of integration. $S_j(t)$ and $\boldsymbol{x}^{c_j}(t)$ indicate respectively the surface and the position of the center of the particles belonging to the generic phase F_j. $n_r(\boldsymbol{y},t)$ denotes the rth component of the outward unit normal $\boldsymbol{n}(\boldsymbol{y},t)$ to the particle surface; finally, $\xi_{ir}(\boldsymbol{y},t)$ is the irth component of the point fluid stress tensor. The last term appearing on the RHS of Eq. 2, $\langle S\rangle_{ik}^{\mathrm{f}}(\boldsymbol{x},t)$, represents the ikth component of the effective fluid stress tensor. Its expression is the following:

$$\langle S\rangle_{ik}^{\mathrm{f}}=\varepsilon\langle\xi_{ik}\rangle^{\mathrm{f}}+n_1\langle s_{ik}^{\mathrm{f}}\rangle^{\mathrm{F}_1}+n_2\langle s_{ik}^{\mathrm{f}}\rangle^{\mathrm{F}_2} -\frac{1}{2}\frac{\partial}{\partial x_m}\left(n_1\langle s_{ikm}^{\mathrm{f}}\rangle^{\mathrm{F}_1}+n_2\langle s_{ikm}^{\mathrm{f}}\rangle^{\mathrm{F}_2}\right)-\varepsilon\rho_{\mathrm{f}}\langle u_i'u_k'\rangle^{\mathrm{f}} \qquad (4)$$

Here $u_i'(\boldsymbol{x},t)$ and $u_k'(\boldsymbol{x},t)$ are the ith and kth components of the fluid velocity fluctuation $\boldsymbol{u}'(\boldsymbol{x},t)$ about the average value $\langle\boldsymbol{u}\rangle^{\mathrm{f}}(\boldsymbol{x},t)$. The term $\varepsilon\rho_{\mathrm{f}}\langle u_i'u_k'\rangle^{\mathrm{f}}(\boldsymbol{x},t)$ is analogous to the "Reynolds stress contribution" in turbulent flow and is representative of the momentum transfer due to the fluctuations of the fluid velocity about its local mean value. The terms $n_1\langle S_{ik}^{\mathrm{f}}\rangle^{\mathrm{F}_1}(\boldsymbol{x},t)$, $n_2\langle S_{ik}^{\mathrm{f}}\rangle^{\mathrm{F}_2}(\boldsymbol{x},t)$, $n_1\langle S_{ikm}^{\mathrm{f}}\rangle^{\mathrm{F}_1}(\boldsymbol{x},t)$, and $n_2\langle S_{ikm}^{\mathrm{f}}\rangle^{\mathrm{F}_2}\ (\boldsymbol{x},t)$ are defined as:

$$n_j\langle s_{ik}^{\mathrm{f}}\rangle^{\mathrm{F}_j}(\boldsymbol{x},t)=a_j\sum_{\mathrm{F}_j}\left\{g\left(\left|\boldsymbol{x}-\boldsymbol{x}^{c_j}\right|\right)\int_{S_j}\xi_{ir}(\boldsymbol{y})n_r(\boldsymbol{y})n_k(\boldsymbol{y})dS_y\right\};\qquad j=1,2 \qquad (5)$$

$$n_j\langle s_{ikm}^{\mathrm{f}}\rangle^{\mathrm{F}_j}(\boldsymbol{x},t) =a_j^2\sum_{\mathrm{F}_j}\left\{g\left(\left|\boldsymbol{x}-\boldsymbol{x}^{c_j}\right|\right)\int_{S_j}\xi_{ir}(\boldsymbol{y})n_r(\boldsymbol{y})n_k(\boldsymbol{y})n_m(\boldsymbol{y})dS_y\right\};\qquad j=1,2 \qquad (6)$$

where a_j is the radius of the particles belonging to phase F_j.

It is evident that finding an analytical closure for the effective fluid stress tensor appears to be a problem of extraordinary complexity; however, a closure has been derived by Jackson[8,9] on theoretical grounds in the limiting case of diluted, Stokesian monocomponent mixtures fluidized by Newtonian fluids. Appropriate closures for the terms on the RHS of Eq. 2 are described later on in the next section (*Closure Relationships* section). We shall now apply the same principles used in deriving the averaged fluid phase equations of motion to the case of the solid phases.

Averaged equations of motion for the particle phase

We now go on to derive the mass and linear momentum averaged equations of conservation for each particle species present in the system. The equations shall be developed by making reference only to phase F_1 as the mathematical manipulations involved are the same for both phases. Since the derivation of the averaged continuity equation is quite straightforward, we shall omit the mathematical details and provide, as already done in the previous section, directly the final result. The equation, expressed in terms of *particle phase averages* (for more detail about this kind of averaging procedure we refer to Jackson[8,9]) takes the form:

$$\frac{\partial n_1}{\partial t} + \frac{\partial}{\partial x_k}\left(n_1 \langle u_k \rangle^{\mathrm{F}_1}\right) = 0 \tag{7}$$

The linear momentum averaged equation of conservation for the particle phase is, conversely, less easy to obtain and presents novel features, which are not found in the original formulation developed by Jackson.[8,9] Accordingly, in the interest of clarity, we shall report in this instance the mathematical derivation in sufficient detail.

In writing the linear momentum equation for the particles present in the binary mixture, Newton's second law of motion is applied. The forces to be taken into consideration include the traction forces exerted by the fluid on the particles, the forces arising as a result of collisions between particles of the same species at their mutual points of contact, those arising as a result of collisions between particles of different species at their mutual points of contact and the effect of gravity. Thus, the linear momentum equation for the generic particle p of phase F_1 takes the form:

$$\begin{aligned}\rho_1 V_1 \frac{du_i^{\mathrm{p}}}{dt} = &\int_{S_1} \xi_{ir}(\boldsymbol{y}) n_r(\boldsymbol{y}) dS_y \\ &+ \sum_{\substack{\mathrm{q}\neq\mathrm{p}\\ \mathrm{q}\in\mathrm{F}_1}} f_i^{\mathrm{pq}} + \sum_{\substack{\mathrm{z}\neq\mathrm{p}\\ \mathrm{z}\in\mathrm{F}_2}} f_i^{\mathrm{pz}} + \rho_1 V_1 g_i\end{aligned} \tag{8}$$

where ρ_1 and V_1 are respectively the density and the volume of the particles of phase F_1, and $u_i^{\mathrm{p}}(t)$ denotes the ith component of the velocity of the center of the generic particle p. The first term on the RHS of Eq. 8 is the overall traction force exerted on the surface of the generic particle p of phase F_1 by the surrounding fluid. The second term is the sum of the direct contact forces $f_i^{\mathrm{pq}}(t)$ exerted on the particle p by the particles q belonging to phase F_1. Finally, the third term is the sum of the direct contact forces $f_i^{\mathrm{pz}}(t)$ exerted on the particle p by the particles z belonging to phase F_2. Indeed the terms $f_i^{\mathrm{pq}}(t)$ and $f_i^{\mathrm{pz}}(t)$ do not vanish only for a limited number of particles, namely those which happen to be in *direct contact* with the particle p at the time t of interest. The third contribution on the RHS of Eq. 8 represents the additional force that has to be taken into account when considering binary mixtures. This term, as we shall see, gives rise to the interphase particle–particle interaction force acting between the two solid phases (which are, in a Eulerian framework, continuous and no longer dispersed).

Equation 8 is averaged by multiplying both sides by $g(|\boldsymbol{x} - \boldsymbol{x}^{c_1}|)$ and by summing over all the particles p belonging to the phase under consideration (in the present instance F_1). Making use of the *particle phase averages* advanced by Jackson[8,9] and the relevant theorems presented by the same author, necessary in the mathematical manipulation of the equation, we obtain:

$$\begin{aligned}\rho_1 V_1 &\left[\frac{\partial}{\partial t}\left(n_1\langle u_i\rangle^{\mathrm{F}_1}\right) + \frac{\partial}{\partial x_k}\left(n_1\langle u_i\rangle^{\mathrm{F}_1}\langle u_k\rangle^{\mathrm{F}_1}\right)\right] \\ &= -\frac{\partial}{\partial x_k}\left(n_1\rho_1 V_1\langle u_i' u_k'\rangle^{\mathrm{F}_1}\right) + n_1\langle f_i^{\mathrm{f}}\rangle^{\mathrm{F}_1} \\ &\quad + n_1\rho_1 V_1 g_i + \sum_{\mathrm{F}_1}\left\{g\left(|\boldsymbol{x}-\boldsymbol{x}^{c_1}|\right)\sum_{\substack{\mathrm{q}\neq\mathrm{p}\\ \mathrm{q}\in\mathrm{F}_1}} f_i^{\mathrm{pq}}\right\} \\ &\quad + \sum_{\mathrm{F}_1}\left\{g\left(|\boldsymbol{x}-\boldsymbol{x}^{c_1}|\right)\sum_{\substack{\mathrm{z}\neq\mathrm{p}\\ \mathrm{z}\in\mathrm{F}_2}} f_i^{\mathrm{pz}}\right\}\end{aligned} \tag{9}$$

The term $n_1\langle f_i^{\mathrm{f}}\rangle^{\mathrm{F}_1}(\boldsymbol{x},t)$ on the RHS of Eq. 9 is the fluid–particle interaction force relevant to phase F_1, which has its exact analog in Eq. 2. The last two terms of the equation, instead, refer respectively to the resultant forces arising from the particle–particle contacts between (a) particles belonging to the same phase and (b) particles belonging to different phases. In consideration of this, such contributions are conceptually different; the former is representative of the stress *internal* to the phase under exam, whereas the second can be interpreted as a contact force acting *between* the two Eulerian solid phases. In order for the solid stress tensor associated to phase F_1 to appear explicitly in Eq. 9, further mathematical manipulations are required; these, again, are a quite simple extension of the mathematical formulation originally advanced by Jackson[8,9] for monocomponent systems and therefore shall be omitted. The result is

$$\begin{aligned}\rho_1 V_1 &\left[\frac{\partial}{\partial t}\left(n_1\langle u_i\rangle^{\mathrm{F}_1}\right) + \frac{\partial}{\partial x_k}\left(n_1\langle u_i\rangle^{\mathrm{F}_1}\langle u_k\rangle^{F_1}\right)\right] \\ &= n_1\langle f_i^{\mathrm{f}}\rangle^{\mathrm{F}_1} + n_1\rho_1 V_1 g_i \\ &\quad + \frac{\partial}{\partial x_k}\left[-n_1\rho_1 V_1\langle u_i' u_k'\rangle^{\mathrm{F}_1} + n_1\langle s_{ik}^{\mathrm{p}}\rangle^{\mathrm{F}_1} - \frac{1}{2}\frac{\partial}{\partial x_m}\left(n_1\langle s_{ikm}^{\mathrm{p}}\rangle^{\mathrm{F}_1}\right)\right] \\ &\quad + \sum_{\mathrm{F}_1}\left\{g\left(|\boldsymbol{x}-\boldsymbol{x}^{c_1}|\right)\sum_{\substack{\mathrm{z}\neq\mathrm{p}\\ \mathrm{z}\in\mathrm{F}_2}} f_i^{\mathrm{pz}}\right\}\end{aligned} \tag{10}$$

where

$$n_1\langle s_{ik}^{\mathrm{p}}\rangle^{\mathrm{F}_1}(\boldsymbol{x},t) = a_1\sum_{\mathrm{F}_1}\left\{g\left(|\boldsymbol{x}-\boldsymbol{x}^{c_1}|\right)\sum_{\substack{\mathrm{q}\neq\mathrm{p}\\ \mathrm{q}\in\mathrm{F}_1}}[f_i^{\mathrm{pq}}(t)n_k^{\mathrm{pq}}(t)]\right\} \tag{11}$$

$$\begin{aligned}n_1\langle s_{ikm}^{\mathrm{p}}\rangle^{\mathrm{F}_1}&(\boldsymbol{x},t) \\ &= a_1^2\sum_{\mathrm{F}_1}\left\{g\left(|\boldsymbol{x}-\boldsymbol{x}^{c_1}|\right)\sum_{\substack{\mathrm{q}\neq\mathrm{p}\\ \mathrm{q}\in\mathrm{F}_1}}[f_i^{\mathrm{pq}}(t)n_k^{\mathrm{pq}}(t)n_m^{\mathrm{pq}}(t)]\right\}\end{aligned} \tag{12}$$

Here $n_k^{\mathrm{pq}}(t)$ and $n_m^{\mathrm{pq}}(t)$ are respectively the kth and mth components of the unit vector:

$$\boldsymbol{n}^{\mathrm{pq}}(t) = \frac{1}{a_1}\left[\boldsymbol{x}^{\mathrm{pq}}(t) - \boldsymbol{x}^{c_1}(t)\right] \tag{13}$$

where $\boldsymbol{x}^{\mathrm{pq}}(t)$ is the position of the point of mutual contact between the particles p and q.

We finally have to tackle the last term on the RHS of Eq. 9. This contribution is representative of the contact force acting between phases F_1 and F_2. Accordingly, the force must fulfil the principle of action and reaction; that is, the following relationship should hold:

$$\begin{aligned} n_1\langle f_i^{\mathrm{p}}\rangle^{\mathrm{F}_1}(\boldsymbol{x},t) &= \sum_{\mathrm{F}_1}\left\{g\left(\left|\boldsymbol{x}-\boldsymbol{x}^{c_1}\right|\right)\sum_{\substack{\mathrm{z}\neq\mathrm{p}\\ \mathrm{z}\in\mathrm{F}_2}} f_i^{\mathrm{pz}}(t)\right\} \\ &= -\sum_{\mathrm{F}_2}\left\{g\left(\left|\boldsymbol{x}-\boldsymbol{x}^{c_2}\right|\right)\sum_{\substack{\mathrm{p}\neq\mathrm{z}\\ \mathrm{p}\in\mathrm{F}_1}} f_i^{\mathrm{zp}}(t)\right\} = -n_2\langle f_i^{\mathrm{p}}\rangle^{\mathrm{F}_2}(\boldsymbol{x},t) \end{aligned} \tag{14}$$

It is not difficult to see that such condition cannot be met. Even if Newton's third law of motion guarantees that $f_i^{\mathrm{pz}}(t)$ is equal and opposite to $f_i^{\mathrm{zp}}(t)$, Eq. 14 is not fulfilled, since $g(|\boldsymbol{x} - \boldsymbol{x}^{c_1}|)$ differs from $g(|\boldsymbol{x} - \boldsymbol{x}^{c_2}|)$. In other words, since in the particle averages of Eq. 14 the forces $f_i^{\mathrm{pz}}(t)$ and $f_i^{\mathrm{zp}}(t)$ *are not given the same weight* (in so much as $\boldsymbol{x}^{c_1} \neq \boldsymbol{x}^{c_2}$), their being equal and opposite does not suffice to render the summations equal to one another in magnitude. This conceptual paradox is very similar to the one encountered by Jackson[8,9] in connection with the interaction force between fluid and particles in monocomponent systems. It is intrinsically related to the way in which the averages are mathematically performed, and directly stems form the use of *particle averages* rather than *solid averages* in the derivation of the macroscopic dynamical equations for the dispersed phases of the system. For more details concerning these alternative averaging procedures, their advantages and drawbacks, and the implications that their employment entails, we refer to Jackson[8,9]. In our specific instance, to overcome the paradox, we operate as follows; we first expand the function $g(|\boldsymbol{x} - \boldsymbol{x}^{\mathrm{pz}}|)$ as a Taylor series in the variable $\boldsymbol{x}^{\mathrm{pz}}(t)$, representative of the position of mutual contact between the generic particle p of phase F_1 and the generic particle z of phase F_2, about the point $\boldsymbol{x}^{c_1}(t)$:

$$\begin{aligned} g\left(\left|\boldsymbol{x}-\boldsymbol{x}^{\mathrm{pz}}\right|\right) &= g\left(\left|\boldsymbol{x}-\boldsymbol{x}^{c_1}\right|\right) - a_1\frac{\partial g\left(\left|\boldsymbol{x}-\boldsymbol{x}^{c_1}\right|\right)}{\partial x_k}n_k^{\mathrm{pz}}(t) \\ &\quad + \frac{1}{2}a_1^2\frac{\partial^2 g\left(\left|\boldsymbol{x}-\boldsymbol{x}^{c_1}\right|\right)}{\partial x_k\partial x_m}n_k^{\mathrm{pz}}(t)n_m^{\mathrm{pz}}(t) - \cdots \end{aligned} \tag{15}$$

where $n_k^{\mathrm{pz}}(t)$ and $n_m^{\mathrm{pz}}(t)$ are respectively the kth and mth components of the unit vector $\boldsymbol{n}^{\mathrm{pz}}(t)$ defined as per Eq. 13. We then introduce Eq. 15 into the LHS of Eq. 14, retaining only the first three terms of the series; this leads to

$$\begin{aligned} \sum_{\mathrm{F}_1}\left\{g\left(\left|\boldsymbol{x}-\boldsymbol{x}^{c_1}\right|\right)\sum_{\substack{\mathrm{z}\neq\mathrm{p}\\ \mathrm{z}\in\mathrm{F}_2}} f_i^{\mathrm{pz}}\right\} &= n_1\langle f_i^{\mathrm{p}}\rangle^{\mathrm{F}_{12}} + \frac{\partial}{\partial x_k}\left(n_1\langle r_{ik}^{\mathrm{p}}\rangle^{\mathrm{F}_1}\right) \\ &\quad - \frac{1}{2}\frac{\partial^2}{\partial x_k\partial x_m}\left(n_1\langle r_{ikm}^{\mathrm{p}}\rangle^{\mathrm{F}_1}\right) \end{aligned} \tag{16}$$

where

$$n_1\langle f_i^{\mathrm{p}}\rangle^{\mathrm{F}_{12}}(\boldsymbol{x},t) = \sum_{\mathrm{F}_1}\left\{g\left(\left|\boldsymbol{x}-\boldsymbol{x}^{\mathrm{pz}}\right|\right)\sum_{\substack{\mathrm{z}\neq\mathrm{p}\\ \mathrm{z}\in\mathrm{F}_2}} f_i^{\mathrm{pz}}(t)\right\} \tag{17}$$

$$n_1\langle r_{ik}^{\mathrm{p}}\rangle^{\mathrm{F}_1}(\boldsymbol{x},t) = a_1\sum_{\mathrm{F}_1}\left\{g\left(\left|\boldsymbol{x}-\boldsymbol{x}^{c_1}\right|\right)\sum_{\substack{\mathrm{z}\neq\mathrm{p}\\ \mathrm{z}\in\mathrm{F}_2}}\left[f_i^{\mathrm{pz}}(t)n_k^{\mathrm{pz}}(t)\right]\right\} \tag{18}$$

$$\begin{aligned} n_1\langle r_{ikm}^{\mathrm{p}}\rangle^{\mathrm{F}_1}(\boldsymbol{x},t) &\\ = a_1^2\sum_{\mathrm{F}_1}&\left\{g\left(\left|\boldsymbol{x}-\boldsymbol{x}^{c_1}\right|\right)\sum_{\substack{\mathrm{z}\neq\mathrm{p}\\ \mathrm{z}\in\mathrm{F}_2}}\left[f_i^{\mathrm{pz}}(t)n_k^{\mathrm{pz}}(t)n_m^{\mathrm{pz}}(t)\right]\right\} \end{aligned} \tag{19}$$

Upon substitution of Eq. 16 into Eq. 10, we have:

$$\begin{aligned} \rho_1V_1\left[\frac{\partial}{\partial t}\left(n_1\langle u_i\rangle^{\mathrm{F}_1}\right) + \frac{\partial}{\partial x_k}\left(n_1\langle u_i\rangle^{\mathrm{F}_1}\langle u_k\rangle^{\mathrm{F}_1}\right)\right] &\\ = \frac{\partial\langle S\rangle_{ik}^{\mathrm{F}_1}}{\partial x_k} + n_1\langle f_i^{\mathrm{f}}\rangle^{\mathrm{F}_1} + n_1\langle f_i^{\mathrm{p}}\rangle^{\mathrm{F}_{12}} + n_1\rho_1V_1g_i& \end{aligned} \tag{20}$$

where the term$\langle S\rangle_{ik}^{\mathrm{F}_1}(\boldsymbol{x},t)$ is defined by:

$$\begin{aligned} \langle S\rangle_{ik}^{\mathrm{F}_1} &= n_1\langle s_{ik}^{\mathrm{p}}\rangle^{\mathrm{F}_1} + n_1\langle r_{ik}^{\mathrm{p}}\rangle^{\mathrm{F}_1} \\ &\quad - \frac{1}{2}\frac{\partial}{\partial x_m}\left(n_1\langle s_{ikm}^{\mathrm{p}}\rangle^{\mathrm{F}_1} + n_1\langle r_{ikm}^{\mathrm{p}}\rangle^{\mathrm{F}_1}\right) - n_1\rho_1V_1\langle u_i'u_k'\rangle^{\mathrm{F}_1} \end{aligned} \tag{21}$$

and denotes the ikth component of the effective stress tensor for the solid phase F_1. The term $n_1\langle f_i^{\mathrm{p}}\rangle^{\mathrm{F}_{12}}$ $(\boldsymbol{x},t)$ fulfills the principle of action and reaction and therefore can be regarded as the effective interphase interaction force between the solid phases. The remaining terms of the Taylor series, which constitute the LHS of Eq. 16 are instead lumped within the effective solid stress tensor of the phase under exam. For completeness, we also report the corresponding averaged equation of conservation for the linear momentum pertaining to phase F_2:

$$\begin{aligned} \rho_2V_2\left[\frac{\partial}{\partial t}\left(n_2\langle u_i\rangle^{\mathrm{F}_2}\right) + \frac{\partial}{\partial x_k}\left(n_2\langle u_i\rangle^{\mathrm{F}_2}\langle u_k\rangle^{\mathrm{F}_2}\right)\right] &\\ = \frac{\partial\langle S\rangle_{ik}^{\mathrm{F}_2}}{\partial x_k} + n_2\langle f_i^{\mathrm{f}}\rangle^{\mathrm{F}_2} + n_2\langle f_i^{\mathrm{p}}\rangle^{\mathrm{F}_{21}} + n_2\rho_2V_2g_i& \end{aligned} \tag{22}$$

where attention should be drawn to the fact that for the principle of action and reaction the following relation holds:

$$n_2\langle f_i^{\mathrm{p}}\rangle^{\mathrm{F}_{21}}(\boldsymbol{x},t) = -n_1\langle f_i^{\mathrm{p}}\rangle^{\mathrm{F}_{12}}(\boldsymbol{x},t) \tag{23}$$

Using the following approximate relationship:

$$\phi_j(\boldsymbol{x},t) = n_j(\boldsymbol{x},t)V_j \tag{24}$$

where ϕ_j $(\boldsymbol{x},t)$ represents the volume fraction of phase F_j, the Eulerian–Eulerian averaged equations of motion for binary-

Table 1. Equations of Motion for a Binary System

Continuity Equation - Fluid Phase

$$\frac{\partial \varepsilon}{\partial t} + \nabla \cdot (\varepsilon \langle \boldsymbol{u} \rangle^{\mathrm{f}}) = 0$$

Continuity Equation - Solid Phase k

$$\frac{\partial \phi_k}{\partial t} + \nabla \cdot (\phi_k \langle \boldsymbol{u} \rangle^{\mathrm{F}_k}) = 0$$

Momentum Equation - Fluid Phase

$$\rho_f \left[\frac{\partial}{\partial t} (\varepsilon \langle \boldsymbol{u} \rangle^{\mathrm{f}}) + \nabla \cdot (\varepsilon \langle \boldsymbol{u} \rangle^{\mathrm{f}} \langle \boldsymbol{u} \rangle^{\mathrm{f}}) \right] = \nabla \cdot \langle \boldsymbol{S} \rangle^{\mathrm{f}} - n_1 \langle \boldsymbol{f}^{\mathrm{f}} \rangle^{\mathrm{F}_1} - n_2 \langle \boldsymbol{f}^{\mathrm{f}} \rangle^{\mathrm{F}_2} + \varepsilon \rho_{\mathrm{f}} \boldsymbol{g}$$

Momentum Equation - Solid Phase 1

$$\rho_1 \left[\frac{\partial}{\partial t} (\phi_1 \langle \boldsymbol{u} \rangle^{\mathrm{F}_1}) + \nabla \cdot (\phi_1 \langle \boldsymbol{u} \rangle^{\mathrm{F}_1} \langle \boldsymbol{u} \rangle^{\mathrm{F}_1}) \right] = \nabla \cdot \langle \boldsymbol{S} \rangle^{\mathrm{F}_1} + n_1 \langle \boldsymbol{f}^{\mathrm{f}} \rangle^{\mathrm{F}_1} + n_1 \langle \boldsymbol{f}^{\mathrm{p}} \rangle^{\mathrm{F}_{12}} + \phi_1 \rho_1 \boldsymbol{g}$$

Momentum Equation - Solid Phase 2

$$\rho_2 \left[\frac{\partial}{\partial t} (\phi_2 \langle \boldsymbol{u} \rangle^{\mathrm{F}_2}) + \nabla \cdot (\phi_2 \langle \boldsymbol{u} \rangle^{\mathrm{F}_2} \langle \boldsymbol{u} \rangle^{\mathrm{F}_2}) \right] = \nabla \cdot \langle \boldsymbol{S} \rangle^{\mathrm{F}_2} + n_2 \langle \boldsymbol{f}^{\mathrm{f}} \rangle^{\mathrm{F}_2} - n_1 \langle \boldsymbol{f}^{\mathrm{p}} \rangle^{\mathrm{F}_{12}} + \phi_2 \rho_2 \boldsymbol{g}$$

fluidized mixtures of solid particles in Newtonian fluids can be summarized, in absolute notation, as shown in Table 1. At first inspection, the analytical form of the final equations does not differ significantly from other formulations already present in literature (this is somewhat encouraging since formally the general expressions of such equations is indeed well established); the method of averaging, however, considerably does. To our knowledge, no other group has applied the averaging scheme put forward by Jackson[8,9] to derive averaged equations of motion for binary systems. In our opinion, the application of such a scheme, along with the various considerations previously presented, adds considerable insight into the meaning of each of the terms featuring in the equations. Moreover, the particle phase method of averaging, which we advocate, seems to us particularly suitable for solid-fluidized suspensions, since, being based on the Lagrangian equations of motion for material bodies, it captures most effectively the physics underlying the dynamics of particulate systems. Appropriate closures, which will be applied to the case studies, will now be discussed in the next section.

Closure Relationships

Effective stress tensor closures

Equations 4 and 21 reveal quite clearly the complex nature of the internal stress associated with each Eulerian phase; this complexity arises from the several different contributions, which ultimately make up the effective stress tensors yielded by the averaging process. This renders the problem of finding appropriate closure relationships, especially based on theoretical grounds, extremely difficult. A vast amount of theoretical research shall probably have to be conducted before the attainment of satisfactory closures. A first approximation commonly employed in the interim is to assume a Newtonian behavior for each continuum, albeit there are clear indications that such a view is over-simplistic. In this approach, the effective stress tensors take the form:

$$\langle \boldsymbol{S} \rangle^{\mathrm{f}} = -\langle p \rangle^{\mathrm{f}} + \mu_{\mathrm{f}} \left[\nabla \langle \boldsymbol{u} \rangle^{\mathrm{f}} + \left(\nabla \langle \boldsymbol{u} \rangle^{\mathrm{f}} \right)^T \right] + \left(\kappa_{\mathrm{f}} - \frac{2}{3} \mu_{\mathrm{f}} \right) \nabla \cdot \langle \boldsymbol{u} \rangle^{\mathrm{f}} \boldsymbol{I} \quad (25)$$

$$\langle \boldsymbol{S} \rangle^{\mathrm{F}_k} = -\langle p \rangle^{\mathrm{F}_k} + \mu_k \left[\nabla \langle \boldsymbol{u} \rangle^{\mathrm{F}_k} + \left(\nabla \langle \boldsymbol{u} \rangle^{\mathrm{F}_k} \right)^T \right] + \left(\kappa_k - \frac{2}{3} \mu_k \right) \nabla \cdot \langle \boldsymbol{u} \rangle^{\mathrm{F}_k} \boldsymbol{I} \quad (26)$$

and the closure problem reduces to finding appropriate constitutive expressions for the pressure $\langle p \rangle$, the shear viscosity μ, and the dilatational viscosity κ pertaining to each phase. The fluid is usually considered incompressible, accordingly its pressure need not be specified constitutively; moreover, μ_{f} is often assumed to be constant and κ_{f} entirely neglected. For the solid phase, conversely, more elaborate constitutive expressions have been developed; some of them, for instance, have been derived from the application of the nonequilibrium kinetic theory for granular gases.[31] Most of these closures, however, cater for monocomponent systems and their extension to binary solid suspensions is not straightforward. In the present work, as customary, the fluid has been assumed incompressible, the shear viscosity constant and equal to that of the pure fluid, and the dilatational viscosity negligible. The internal stress associated with the solid, on the other hand, has not been accounted for due to the lack of fully-validated equations of closures in literature.

Fluid–particle interaction force closures

The fluid–particle interaction force accounts for the resultant force, which is exerted by the fluid on the particles of phase F_k. In this work, this force is assumed to be made up of three contributions, namely buoyant force, drag force, and elastic force:

$$n_k \langle \boldsymbol{f}^{\mathrm{f}} \rangle^{\mathrm{F}_k} = n_k \langle \boldsymbol{f}^{s} \rangle^{\mathrm{F}_k} + n_k \langle \boldsymbol{f}^{d} \rangle^{\mathrm{F}_k} + n_k \langle \boldsymbol{f}^{e} \rangle^{\mathrm{F}_k} \quad (27)$$

It is worth pointing out that other contributions to the fluid–particle interaction force should, at least in principle, be considered; we mention, for instance, the virtual mass force, the lift force, the Faxen force, and a history-dependent term analogous to the Basset force for the motion of isolated particles. In the present analysis, however, these additional contributions have all been neglected. With regard to the latter, it seems reasonable to believe that for dense fluidized suspensions, the space-averaging of history-dependent forces would result into a vanishing contribution; indeed, the averaging procedure would most probably erase any historical effect of the motion of the particles on the fluid in their immediate neighbourhood.[7,32] For all the remaining contributions, exact expressions have been derived analytically by some authors for the case of *single particles* (usually of spherical or nearly spherical shape) in nonuniform flows. These closures, however, apply to very specific fluid dynamic conditions; for instance, vanishing or very low Reynolds numbers.[33,34] These results have been used more recently by some researchers to develop analytically space-averaged closures catering for solid monocomponent-fluidized suspensions; we mention, for instance, the work of Zhang and Prosperetti[35,36] and Jackson.[8,9] These expressions, however, are applicable under very restricting assumptions such as vanishing viscosity,[35] small Stokes and Reynolds numbers[8,9,36] or low particle concentrations.[8,9,35,36] Generalizing these expressions to other fluid dynamic conditions is by no means straightforward and often raises conceptual issues (related, for example, to frame indifference and objectivity). It is interesting to report, for example, that the lift force on an *isolated spherical* particle takes quite different functional forms in the inviscid and low Reynolds number cases[32,37,38]; thus, finding an expression of general validity for a space-averaged closure of such term still appears, for the time being, to be a daunting task. The virtual mass force, conversely, has a quite well established functional form, even if empirical expressions for a concentration-dependent virtual mass coefficient are still to be found. In light of these considerations, as already said, forces other than those retained in Eq. 27 have been neglected; this approximation is indeed anything but uncommon and is found in the work of several research groups.[22,24,31,39–42]

We now describe the closures used in the present work to express the three contributions to the fluid–particle interaction force reported in Eq. 27. The *buoyant force* associated to the phase F_k is related to the isotropic part of the effective fluid stress tensor and the solid volume fraction ϕ_k as follows:

$$n_k \langle \boldsymbol{f}^s \rangle^{\mathrm{F}_k} = -\phi_k \nabla \langle p \rangle^{\mathrm{f}} \tag{28}$$

Equation 28 is a generalization of one of the closures commonly used for such a force. The *drag force* is expressed, as usual, as the product of a drag coefficient β_k and the relative slip velocity between the fluid and the particle phase of interest.

$$n_k \langle \boldsymbol{f}^d \rangle^{\mathrm{F}_k} = \beta_k \left(\langle \boldsymbol{u} \rangle^{\mathrm{f}} - \langle \boldsymbol{u} \rangle^{\mathrm{F}_k} \right) \tag{29}$$

Here the closure used for the interphase momentum transfer coefficient is that derived by Owoyemi,[43] and Owoyemi and Lettieri[44] from an expression originally advanced by Di Felice[45] for the unrecoverable pressure drop per unit length in a suspension. The expression is applicable for both fixed and fluidized beds and has the form

$$\beta_k = \left[\left(\frac{17.3}{Re_k} \right)^{\alpha} + (0.336)^{\alpha} \right]^{\frac{1}{\alpha}} \frac{\rho_{\mathrm{f}} \left| \langle \boldsymbol{u} \rangle^{\mathrm{f}} - \langle \boldsymbol{u} \rangle^{\mathrm{F}_k} \right| \phi_k}{d_k} \varepsilon^{-1.8} \tag{30}$$

where d_k is the diameter of the particles of phase F_k. The Reynolds number and the exponent α are given by

$$Re_k = \frac{\rho_{\mathrm{f}} \varepsilon \left| \langle \boldsymbol{u} \rangle^{\mathrm{f}} - \langle \boldsymbol{u} \rangle^{\mathrm{F}_k} \right| d_k}{\mu_{\mathrm{f}}}; \tag{31}$$

$$\alpha = 2.55 - 2.1 \left[\tanh (20\varepsilon - 8)^{0.33} \right]^3 \tag{32}$$

The *elastic force* is a specific feature of the present model. The concept of elasticity associated to multiphase flow, and in particular to solid fluidized suspensions, was initially introduced by Wallis[30] and thereafter further developed by Foscolo and Gibilaro,[46] and Gibilaro.[47] It originally stems from a theoretical investigation into the hydrodynamic stability of homogeneous fluidized beds. The first formulation of the averaged linear momentum equations of conservation, and more specifically of the fluid–particle interaction force featuring in them and comprising solely the drag and the buoyant forces, leads to an intrinsic instability of the homogeneous state of fluidization. The inclusion of additional contributions to the interaction force such as those previously discussed (virtual mass force, lift force and the like) does not bring about any significant qualitative change. This appears to be inconsistent with experimental evidence; there are, in fact, many systems (fluidized by either gas or liquid) that are found to expand in an unambiguously homogeneous fashion (at least, from what can be experimentally observed) up to a critical, often well-defined value of the fluid volume fraction. The physical arguments put forward by Foscolo and Gibilaro[46] led to the introduction of an additional force, the elastic force, related to the gradients in the suspension void fraction, which are generated when the homogeneity of the system is lost at the macroscopic length scale. The inclusion of this contribution into the fluid–particle interaction force results into a simple criterion for discriminating between stable and unstable fluidization. The original formulation of the elastic force closure, developed for monodimensional systems of monosized particles near equilibrium conditions, is not adequate, however, for the study of the dynamics of fluidized suspensions far from equilibrium. A revised, multidimensional, and somewhat generalized formulation of the force has been subsequently advanced by Mazzei et al.[48] for monocomponent systems. The force is therein regarded as a component of the drag force; more specifically, the contribution related to voidage gradients within the suspension, which arise under nonequilibrium conditions. The approach of Mazzei et al.[48] has then been adopted and extended by Owoyemi,[43] and Owoyemi and Lettieri[44] for binary mixtures; the closure takes the following expression:

$$n_k \langle \boldsymbol{f}^e \rangle^{\mathrm{F}_k} = E_k \left(\nabla \varepsilon \cdot \langle \boldsymbol{n}^d \rangle^{\mathrm{F}_k} \right) \langle \boldsymbol{n}^d \rangle^{\mathrm{F}_k} \tag{33}$$

where $\langle \boldsymbol{n}^d \rangle^{\mathrm{F}_k}$ is the unit drag force vector pertaining to the solid phase F_k, the *elastic modulus* E_k is given by

$$E_k = -\frac{2}{3} d_k \left[\left(-\frac{3.8}{\varepsilon} + \chi \right) \left| n_k \langle \boldsymbol{f}^d \rangle^{\mathrm{F}_k} \right| - \phi_k (\rho_k - \rho_{\mathrm{f}}) g \right] \tag{34}$$

and the functional form of χ is

$$\chi = \frac{1}{\alpha}\left\{-\frac{1}{\alpha}\ln\left[\left(\frac{17.3}{Re_k}\right)^{\alpha} + (0.336)^{\alpha}\right] + \frac{\left(\frac{17.3}{Re_k}\right)^{\alpha}\ln\left(\frac{17.3}{Re_k}\right) + (0.336)^{\alpha}\ln(0.336)}{\left(\frac{17.3}{Re_k}\right)^{\alpha} + (0.336)^{\alpha}}\right\} \times\left\{6.3\left[\tan\text{h}\,(20\varepsilon - 8)^{0.33}\right]^{2}\right\}\{\sec\text{h}^{2}(20\varepsilon - 8)^{0.33}\}\{6.6(20\varepsilon - 8)^{-0.67}\} \quad (35)$$

Particle–particle interaction force closures

In the present model, the only constituent of the particle–particle interaction force, which has been taken into consideration, is the interphase drag. The force is expressed as the product of a drag coefficient ζ and the relative slip velocity between the two solid phases:

$$n_1\langle \boldsymbol{f}^{\text{p}}\rangle^{\text{F}_{12}} = \zeta\left(\langle \boldsymbol{u}\rangle^{\text{F}_2} - \langle \boldsymbol{u}\rangle^{\text{F}_1}\right) = -n_2\langle \boldsymbol{f}^{\text{p}}\rangle^{\text{F}_{21}} \quad (36)$$

Several investigators have put forward empirical correlations to account for the momentum transfer coefficient ζ. In this article, three drag constitutive equations proposed by Gidaspow et al.,[20] Bell,[21] and Syamlal[29] have been compared. A summary of the closure relationships proposed by these researchers is given in Table 2. In the correlation advanced by Syamlal,[29] the radial distribution function g_o derived by Lebowitz[49] was used.

Solid phase compaction control

As previously pointed out, in the present work, the internal stress associated with the solid phases has been neglected. This might give rise to local over-compaction in some regions of the simulated fluidized bed. To counter this effect, a new numerical algorithm has been developed. The new numerical scheme is based on the algorithm for the *excess solid volume correction* originally developed by Lettieri et al.[50] for monocomponent systems. In the original algorithm, the redistribution of the solid volume in excess within each cell of the computational grid is carried out after each time step for cells where the solid volume fraction ϕ is greater than the maximum compaction value $\phi^{\max}$ set by the user. The correction is expressed in terms of volume and not mass, since the system is assumed incompressible. The redistribution of the excess volume, defined as $\phi^{\text{ex}} = \phi - \phi^{\max}$, is in the form of an overall volume balance for the particle phase and is active within each cell where the overpacking condition is detected. In a 2D computational domain with cells of equal size, the cell in question gives away its overall particle phase volume excess to the neighboring cells in equal parts, i.e. the excess divided by the number of neighbouring cells, and in turn receives the relevant part of the excess coming from the neighbouring cells. The corrected value of the solid volume fraction in the cell is then computed on the basis of the value provided by the code and the net excess solid volume exchanged between the cell under exam and the neighboring ones (Figure 1). The balance may be expressed in terms of solid volume fraction, since all the cells have the same volume.

$$\phi_{i,j}^{\text{new}} = \phi_{i,j}^{\text{old}} - \phi_{i,j}^{\text{ex}} + \frac{\phi_{i+1,j}^{\text{ex}}}{4} + \frac{\phi_{i,j+1}^{\text{ex}}}{4} + \frac{\phi_{i-1,j}^{\text{ex}}}{4} + \frac{\phi_{i,j-1}^{\text{ex}}}{4} \quad (37)$$

In the present work, the original algorithm has been extended for the case of binary systems. The new algorithm allows dynamic calculation of the total maximum solid-packing $\phi_{12}^{\max}$ in each cell within the computational grid after each time step. The parameter $\phi_{12}^{\max}$ is equal to

$$\phi_{12}^{\max} = \phi_1^{\max} + \phi_2^{\max} \quad (38)$$

where $\phi_1^{\max}$ and $\phi_2^{\max}$ denote the local (i.e., relative to the cell under exam) maximum value of the solid volume fractions ϕ_1 and ϕ_2 of phases F_1 and F_2, respectively. These two parameters are not known a priori but are computed by the algorithm. The computation of the instantaneous total maximum solid-packing is also necessary because each cell of the computational domain contains a unique distribution of particles, which varies in time and from cell to cell. The dynamic control for $\phi_{12}^{\max}$ is achieved by implementing the equation proposed by Fedors and Landel[51] for the maximum solid-packing in a binary mixture of spheres reported in Table 2. The numerical solid compaction algorithm is described as follows and shown diagrammatically in Figure 2.

1. The maximum allowable solid compaction Φ_1 and Φ_2 are set manually, e.g. to the value of 0.60, for both phases F_1 and F_2 present in the mixture.
2. The algorithm collects, as an input, the values of the local solid volume fractions ϕ_1^{old} and ϕ_2^{old} at the current time step. The values are then used to compute the local maximum solid volume fraction $\phi_{12}^{\max}$ for the mixture, in each computational cell, using the Fedors and Landel[51] equation.
3. The calculated maximum packing volume fraction for the mixture is then shared between phases F_1 and F_2 using a simple redistribution based on proportionality. The above enables the calculation of the excess volume fractions ϕ_1^{ex} and ϕ_2^{ex}.
4. The new corrected solid volume fractions ϕ_1^{new} and ϕ_2^{new} for each phase is then calculated using Eq. 37.

It is worth noting that the algorithm does not necessarily drop the excess solid volume out of the cell, but it rather rearranges the solid volume field so that the solid volume excess is transported toward regions of the computational domain where no excess is present.

The strength of this procedure lies in the implementation of a *local* numerical correction of the solid volume fraction only in the computational cells where this is required, without the introduction of additional terms in the equations of motion (such as additional pressure gradients for the solid phases) whose closures are still for the time being not entirely reliable and which would affect the numerical solution *globally*.[50]

Table 2. Particle–Particle Drag Models Used in This Work

Gidaspow et al.[20]

$$\zeta = F(1+e)\frac{\phi_1\rho_1\phi_2\rho_2(d_1+d_2)^2}{\rho_1 d_1^3+\rho_2 d_2^3}\left|\langle \boldsymbol{u}\rangle^{\mathrm{F}_1}-\langle \boldsymbol{u}\rangle^{\mathrm{F}_2}\right|$$

$$F = \frac{3(\phi_{12}^{\max})^{1/3}+(\phi_1+\phi_2)^{1/3}}{4\left[(\phi_{12}^{\max})^{1/3}-(\phi_1+\phi_2)^{1/3}\right]}$$

Syamlal[29]

$$\zeta = \frac{3(1+e)\left(\frac{\pi}{2}+C_{\mathrm{f}}\frac{\pi^2}{8}\right)\phi_1\rho_1\phi_2\rho_2(d_1+d_2)^2 g_{\mathrm{o}}}{2\pi(\rho_1 d_1^3+\rho_2 d_2^3)}\left|\langle \boldsymbol{u}\rangle^{\mathrm{F}_1}-\langle \boldsymbol{u}\rangle^{\mathrm{F}_2}\right|$$

$$g_{\mathrm{o}} = \frac{1}{\varepsilon}+\frac{3}{\varepsilon^2}\frac{d_1 d_2}{(d_1+d_2)}\left(\frac{\phi_1}{d_1}+\frac{\phi_2}{d_2}\right)$$

Bell[21]

$$\zeta = \frac{2(1+e)\phi_1\rho_1\phi_2\rho_2(d_1+d_2)^2\left[1+\frac{3}{4}\left(\frac{\phi_{12}^{\max}}{\phi_1+\phi_2}\right)^{1/3}\right]}{(\rho_1 d_1^3+\rho_2 d_2^3)\left(\frac{\phi_{12}^{\max}}{\phi_1+\phi_2}\right)^{1/3}}\left|\langle \boldsymbol{u}\rangle^{\mathrm{F}_1}-\langle \boldsymbol{u}\rangle^{\mathrm{F}_2}\right|$$

The parameter $\phi_{12}^{\max}$ is assessed using the Fedors and Landel[51] equation:

$$a=\sqrt{\frac{d_2}{d_1}};\quad X_{12}=\frac{\phi_1}{\phi_1+\phi_2}$$

$$\phi_{12}^{\max}=[(\Phi_1-\Phi_2)+(1-a)(1-\Phi_1)\Phi_2][\Phi_1+(1-\Phi_1)\Phi_2]\frac{X_{12}}{\Phi_1}+\Phi_2$$

$$\text{for}\quad X_{12}\le\frac{\Phi_1}{\Phi_1+(1-\Phi_1)\Phi_2}$$

$$\phi_{12}^{\max}=(1-a)[\Phi_1+(1-\Phi_1)\Phi_2](1-X_{12})+\Phi_1$$

$$\text{for}\quad X_{12}\ge\frac{\Phi_1}{\Phi_1+(1-\Phi_1)\Phi_2}$$

The indices 1 and 2 must be chosen so that the following condition holds: $d_1 \ge d_2$; Φ_1 and Φ_2 are the maximum values for ϕ_1 and ϕ_2, respectively.

Simulations

In the present study, all the simulations were carried out using a commercial CFD package, CFX 4.4. The governing equations described in Table 1 as well as all the closure relations reported in *Closure Relationships* section were implemented in the code. A 2D computational grid, in which front and back wall effects are neglected, was used. The left and right walls of the domain were modeled using no-slip velocity boundary conditions for all phases. Dirichlet boundary conditions were employed at the bottom of the bed to specify a uniform gas inlet velocity. A pressure boundary condition was specified at the top of the bed and set to a reference value of 1.015×10^5 Pa. The distributor was made impenetrable to the solid phase. A second-order discretization scheme, SUPERBEE, was used for all equations to improve the computational prediction of bubble shape and behavior.[52] A total of four different simulations was carried out. The fluidized bed was initially filled in two layers in which the flotsam particles (smaller particles) occupied the bottom half of the bed, whilst the jetsam particles (bigger particles) occupied the top half of the bed. The particle–particle drag constitutive equations shown in Table 2 were implemented for three of the cases. A fourth reference simulation was carried out in which no particle–particle drag was accounted for. All simulations were performed for a total of 10 s of real time (this is roughly twice the time required by the simulated system to achieve steady-state conditions). The simulations were carried out using three Dual Processor Dell Xeon P4 3.2 GHz machines. Computational parameters and fluidization conditions used for the simulations are summarized in Table 3. The grid resolution and time step adopted were based on a previous work by Lettieri et al.[53] The values used are in concurrence with figures recommended by several other researchers. We mention, in this regard, the work by Samuelsberg and Hjertager,[54] Enwald and Almstedt,[55] van Wachem,[56] Mathiesen et al.,[57] and McKeen and Pugsley[58] to name just a few. In the works referred to, the cells size

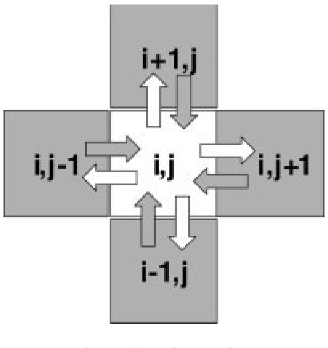

Figure 1. Computational domain representation of excess volume correction.

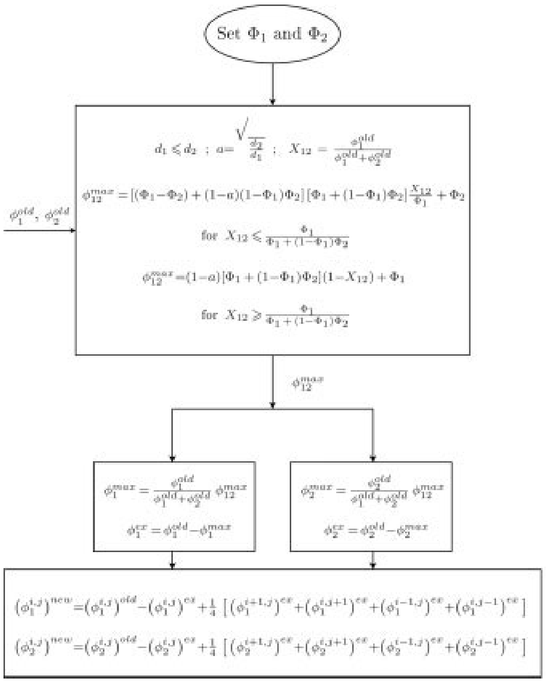

Figure 2. Solid compaction correction algorithm.

Table 3. Computational Parameters Used in the CFD Simulations

Description	Symbol	Value	Units	Comments
Gas density	ρ_f	1.29	kg/m^3	
Gas viscosity	μ_f	1.85×10^{-5}	Pa s	
Bed height	H_b	0.60	m	
Settled bed height	H_s	0.30	m	
Grid cell size	Δx and Δy	0.005	m	Square cells
Time step	Δt	10^{-4}	s	
Superficial gas velocity	U_o	0.25	m/s	
Coefficient of restitution	e	0.97	–	Syamlal[29]
Coefficient of friction	C_f	0.15	–	Syamlal[29]

length is usually of the order of 1 cm (varying between 0.5 and 4.0 cm); the time step (when specified) is in the range $1.0E-04$ s to $1.0E-02$ s. In our study, the choice of using a grid resolution of 0.5 cm and a time step of $1.0E-04$ s is therefore conservative and should be adequate and sufficiently small.

Experimental

The experimental set-up used in this work, shown in Figure 3, consists of a two-dimensional Plexiglas rectangular column, 600-mm high, 350-mm wide, and 10-mm thick. The distributor is a uniformly permeable sintered bronze rectangular plate with a thickness of 3.5 mm. The fluidizing gas, air, is supplied via rotameters. The gas is dehumidified and filtered to remove possible impurities present in the stream. Pressure taps are installed 100 mm apart along the height of the bed from which pressure readings are collected via an electronic manometer. A system of two interlocked on/off valves operated simultaneously is installed on the rig to allow for instantaneous evacuation of the fluidizing gas during the bed freeze tests performed for the analysis of the mixing and segregation that occurs in the bed.

The binary system investigated is characterized by components that differ in size and have the same density. Ballotini powder samples (PSD reported in Figures 4 and 5) with mean particle diameter of 200 μm and 350 μm respectively and density of 2500 kg/m^3 were used in the fluidization experiments. The larger and smaller ballotini particles represent the *jetsam* and *flotsam* particles, respectively. The bed is initially completely segregated. The flotsam particles are filled first up to a height of 150 mm; the jetsam particles are then added on top up to a height of 300 mm. This corresponds to 0.88 and 0.97 kg of the flotsam and jetsam particles, respectively.

The experiments were carried out at a superficial gas velocity U_o of 0.25 m/s. This value was determined using the procedure described below based on two semiempirical correlations. The first correlation is the one derived by Wu and Baeyens,[19] which relates an index M representative of the

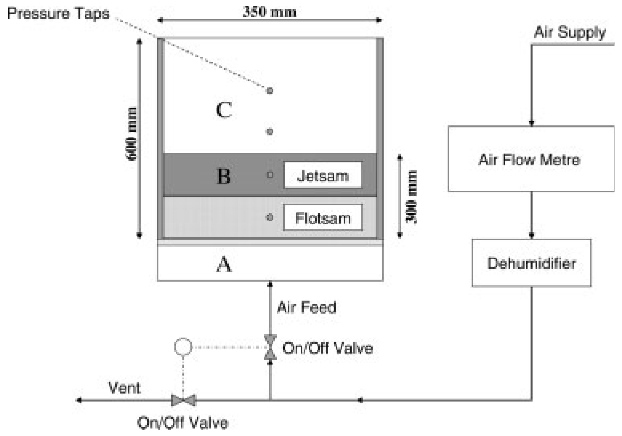

Figure 3. Experimental apparatus: (A) Windbox; (B) Fluidized bed; (C) Freeboard.

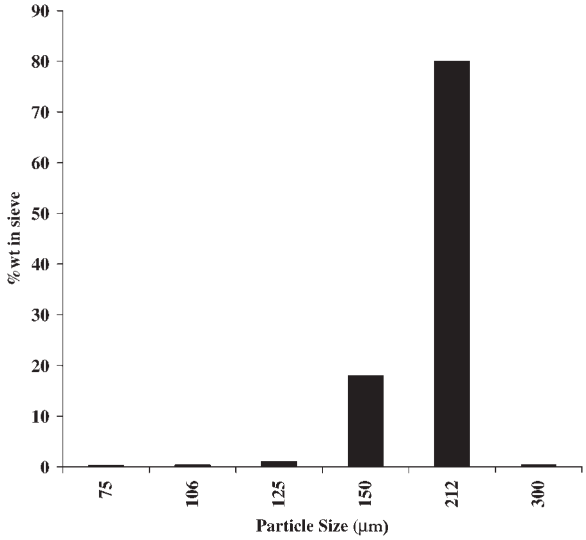

Figure 4. Particle size distribution of the flotsam powder.

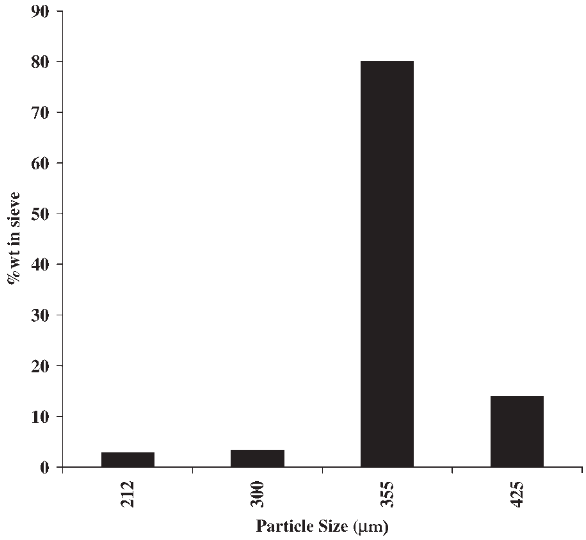

Figure 5. Particle size distribution of the jetsam powder.

bed mixedness (whose formal definition is given in *Mixing and Segregation* section under *Results and Discussion* section) to the visible bubble flow rate Q_B/A throughout the bed, which is thought to be the real driving force behind mixing and segregation:

$$M = 1 - 0.0067 d_{\mathrm{R}} 1.33 \left(\frac{Q_B}{A}\right)^{-0.75} \tag{39}$$

In this last equation, d_{R} is the ratio d_1/d_2 of the larger diameter to the smaller diameter of the particles. The second correlation was used to evaluate Q_B/A and is a modification of the original correlation derived in the *two-phase theory of fluidization* proposed by Toomey and Johnstone[59] and successively developed by Davidson and Harrison.[60] The modified correlation takes the form:

$$\frac{Q_B}{A} = \gamma(U_{\mathrm{o}} - U_{\mathrm{mf}}) \tag{40}$$

where U_{mf} is the minimum fluidization velocity of the system and γ is a *throughflow* empirical corrective factor. The two-phase theory was a first attempt at quantifying Q_B/A. The theory modeled a fluidized bed as consisting of an emulsion phase of voidage $\varepsilon_{\mathrm{mf}}$, wherein the fluid flow rate is equal to that at incipient fluidization conditions and a bubble phase, which carries the additional flow of fluid. The visible bubble flow rate was considered to be equal to the excess gas flow above that required for minimum fluidization, i.e. $\gamma = 1$ in Eq. 40. It was noted, however, that in practice Q_B/A was rather smaller than the one predicted by the original theory. This led to the introduction of the corrective factor γ featuring in Eq. 40. In the present work, the empirical correlation for γ advanced by Wu and Baeyens[19] has been used:

$$\gamma(Ar) = \begin{cases} 1 & \text{for } \; Ar \le 50 \\ 2.27 Ar^{-0.21} & \text{for } \; Ar > 50 \end{cases} \tag{41}$$

where the Archimedes number Ar of the mixture is given by

$$Ar = \frac{\rho_m - \rho_{\mathrm{f}}}{\rho_{\mathrm{f}}} Ga; \quad \frac{1}{\rho_m} = \frac{\omega_1}{\rho_1} + \frac{\omega_2}{\rho_2} \tag{42}$$

and the Galileo number Ga is equal to

$$Ga = \frac{d_m^3 \rho_{\mathrm{f}}^2 g}{\mu_{\mathrm{f}}^2}; \quad d_m = \frac{\omega_1 \rho_2 + \omega_2 \rho_1}{\omega_1 \rho_2 d_2 + \omega_2 \rho_1 d_1} d_1 d_2 \tag{43}$$

In Eqs. 42 and 43, the quantities ω_1 and ω_2 denote the mass fractions of the larger and smaller particles respectively in the powder devoid of fluid; these therefore take the expressions:

$$\omega_1 = \frac{\phi_1 \rho_1}{\phi_1 \rho_1 + \phi_2 \rho_2}; \quad \omega_2 = \frac{\phi_2 \rho_2}{\phi_1 \rho_1 + \phi_2 \rho_2} \tag{44}$$

The minimum fluidization velocity U_{mf} of the mixture was calculated using the correlation proposed by Gossens et al.[61]:

$$U_{\mathrm{mf}} = \frac{\mu_{\mathrm{f}}}{\rho_{\mathrm{f}} d_m} \left[(33.7^2 + 0.0408 Ar)^{0.5} - 33.7 \right] \tag{45}$$

Equations 39 and 40 were used to calculate the superficial gas velocity U_{o} as follows: (a) the desired mixing index M was chosen and the visible bubble flow rate was evaluated from Eq. 39; (b) the minimum fluidization velocity U_{mf} of the mixture was then gauged using Eq. 45; (c) the superficial gas velocity U_{o} was finally assessed using Eq. 40. In the present work, an arbitrary value of 0.9 was chosen for the mixing index M; this corresponds to a state of almost perfect mixing within the bed, as it will be further discussed in *Mixing and Segregation* section under *Results and Discussion* section.

Digital video recordings of the fluid bed were made to analyze the development of the bubble dynamics within the bed and to determine the bubble size at the operating conditions employed. Images captured by means of a web camera at 14 frames/s for 80 s were recorded and subsequently analyzed using Optimas 6.0, an image analysis software.

A bed freeze analysis, for the experimental investigation of mixing and segregation, was conducted 1 min after the initiation of the experiments (time required by the real system to achieve steady-state conditions). In the bed freeze tests, the fluidizing air supply was shut off abruptly. The bed at rest was then split into four horizontal layers and each layer was sieved to obtain the percentage by weight of the different components. Samples used for sieving in this work were collected by means of a probe attached to a vacuum pump. Results of the bed freeze analysis are reported in Table 4 and Figures 6 and 7 and shall be discussed later on.

Results and Discussion

Mixing and segregation

A proper description of the state of particle distribution in a binary gas-fluidized bed can be achieved by means of two established parameters, the mixing index M and the coefficient of segregation C_s. The use of either depends on the approach of interest. If the mixedness of the system is of primary concern, then the mixing index is more appropriate; if, on the other hand, the degree of segregation is of direct interest, then the coefficient of segregation is more suitable. The two however, even if not directly related, should ultimately provide the same physical information. The mixing index was first defined by Rowe et al.[62] as:

Table 4. Experimental and Theoretical Values of the Mixing Index M and the Coefficient of Segregation C_s for All Simulations

Drag Model	Mixing Index	Coefficient of Segregation
Experimental	0.886	+3.520
Wu and Baeyens[19]	0.900	–
Bell[21]	0.972	+2.456
Gidaspow et al.[20]	0.984	+1.312
Syamlal[29]	0.999	−0.620
No particle drag implemented	0.637	+17.177

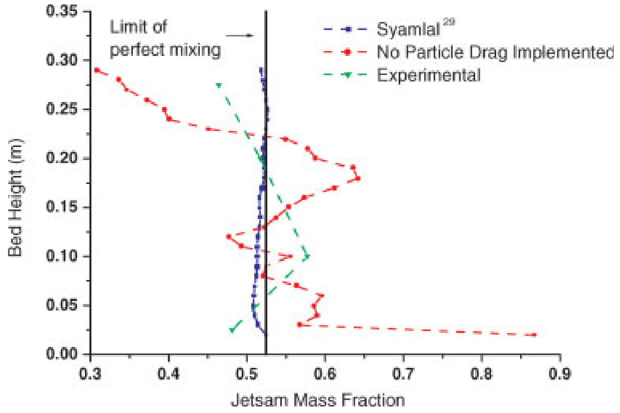

Figure 6. Comparison of computational and experimental segregation patterns.

[Color figure can be viewed in the online issue, which is available at www.interscience.wiley.com.]

$$M = \frac{\langle \omega_{\mathrm{jet}} \rangle_{\mathrm{t}}}{\langle \omega_{\mathrm{jet}} \rangle_{\mathrm{o}}} \tag{46}$$

where $\langle \omega_{\mathrm{jet}} \rangle_{\mathrm{t}}$ is the average mass fraction of the jetsam phase in the top region of the bed and $\langle \omega_{\mathrm{jet}} \rangle_{\mathrm{o}}$ is the average mass fraction of the jetsam phase evaluated over the entire bed. The top region of the bed is not uniquely defined, but can be chosen somewhat arbitrarily. Here, following van Wachem et al.,[24] the region was assumed to be the top 25% of the bed. The above definition intrinsically equates a state of perfect jetsam segregation *at the bottom of the bed* to a mixing index of $M = 0$ and a state of perfect mixing to a mixing index of $M = 1$. Perfect jetsam segregation *at the top of the bed*, which is usually imposed before the system is fluidized, is instead given by a mixing index of $M = (m_{\mathrm{jet}} + m_{\mathrm{flot}})/m_{\mathrm{jet}}$, where m_{jet} and m_{flot} are the overall masses of jetsam and flotsam in the bed, respectively. In the present case, since $m_{\mathrm{jet}} = 0.97$ kg and $m_{\mathrm{flot}} = 0.88$ kg, the index varies between 0 and 1.91. The coefficient of segregation, introduced by Geldart,[63] is given by:

$$C_s = \frac{\langle \omega_{\mathrm{jet}} \rangle_{\mathrm{b}} - \langle \omega_{\mathrm{jet}} \rangle_{\mathrm{t}}}{\langle \omega_{\mathrm{jet}} \rangle_{\mathrm{b}} + \langle \omega_{\mathrm{jet}} \rangle_{\mathrm{t}}} \cdot 100 \tag{47}$$

where $\langle \omega_{\mathrm{jet}} \rangle_{\mathrm{b}}$ and $\langle \omega_{\mathrm{jet}} \rangle_{\mathrm{t}}$ are the mass fractions of the jetsam phase in the bottom and top halves of the bed. Clearly C_s varies between -100 and $+100$, with -100 denoting perfect jetsam segregation at the top of the bed, 0 being representative of perfect mixing, and $+100$ indicating perfect jetsam segregation at the bottom of the bed.

Table 4 reports the mixing index M and the coefficient of segregation C_s calculated from experiments and after 10 s of simulation for all the different case studies examined. The values of M are also compared with the prediction obtained from the semiempirical correlation developed by Wu and Baeyens[19] and presented formerly in the *Experimental* section. All the simulations show a reasonably good agreement with the experimental data and the semitheoretical expression with the exception of the case where the particle–particle drag was neglected. In quantitative terms, as regards the mixing index, the correlation by Wu and Baeyens[19] yields predictions, which deviate from experimental measurements by 1.6%, the numerical simulations accounting for the particle–particle drag present a deviation in the range 9% (Bell[21] closure)–13% (Syamlal[29] closure), whereas when the foregoing contribution is neglected a percent error is found in excess of 28%. The theoretical results obtained when the particle–particle drag is accounted for are not noticeably affected by the specific closure adopted and always appear to slightly overpredict the degree of mixing within the bed. In particular, the equation by Syamlal[29] yields an almost perfect mixing with a mixing index of roughly 1. Conversely, in the reference simulation, where no drag force is implemented, the segregation of the jetsam phase is somewhat overestimated as clearly indicated by the low mixing index and high coefficient of segregation obtained in this instance. In the light of these results, it seems reasonable to conclude that the absence of particle–particle drag causes the jetsam phase to migrate swiftly toward the bottom of the bed on account of the lack of hindrance (friction) that would otherwise have hampered this motion.

Figures 6 and 7 show a comparison between theoretical and experimental concentration profiles of the jetsam phase throughout the bed. The computational values were determined after 10 s of simulation by splitting the bed into 28 horizontal layers of equal volume and by calculating the average jetsam mass fraction in each layer. The experimental results were obtained as described earlier on in *Experimental* section; in this case, only four horizontal layers were considered. The profiles shown are consistent with the figures reported in Table 4 and confirm the conclusions previously drawn. In the case study, where the Syamlal[29] equation was used, we find an almost flat vertical profile with a constant jetsam mass fraction throughout the bed equal to roughly 0.52. This corresponds to a state of almost perfect mixing where the jetsam mass fraction would be equal to $\langle \omega_{\mathrm{jet}} \rangle_{\mathrm{o}} = 0.97/(0.97 + 0.88) = 0.524$. The degree of mixing is also slightly overestimated in the case studies where the equations of closure by Gidaspow et al.[20] and Bell[21] were used. Here,

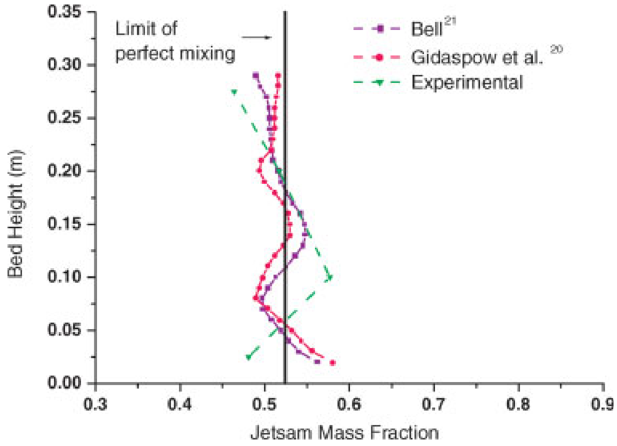

Figure 7. Comparison of computational and experimental segregation patterns.

[Color figure can be viewed in the online issue, which is available at www.interscience.wiley.com.]

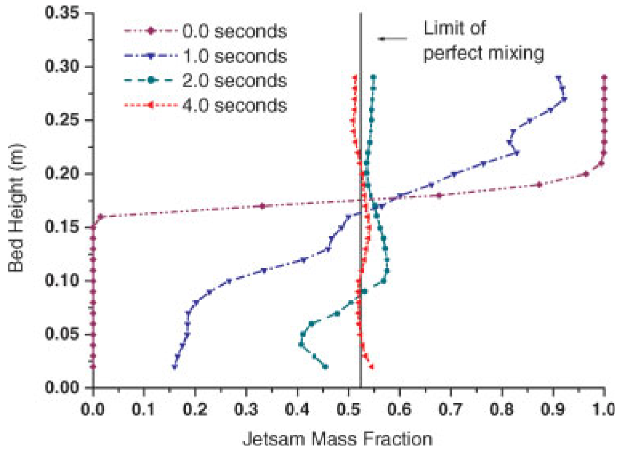

Figure 8. Evolution of the jetsam mass fraction profile with time obtained using the Syamlal[29] drag correlation.

[Color figure can be viewed in the online issue, which is available at www.interscience.wiley.com.]

as expected, the jetsam mass fraction profiles almost overlap with the limit of perfect mixing, with a jetsam concentration on the bottom of the bed slightly higher than on top. This is in agreement with the values of M and C_s formerly calculated and shown in Table 4. The effect due to lack of hindrance on the jetsam phase is again clearly found when no particle–particle drag was considered. In this instance, the jetsam distribution throughout the bed is highly uneven. In the upper region of the bed, the jetsam mass fraction drops to values as low as 0.3 and the profile lies on the left of the limit of perfect mixing. In the remainder of the bed, conversely, the jetsam concentration is appreciatively higher, the profile shifts to the right of the limit of perfect mixing, and the mass fraction reaches values up to 0.66. This is clearly indicative of a state of segregation within the bed and confirms what was previously found from the analysis of the segregation and mixing parameters. This prediction is in sharp contrast with the experimental findings, which present a jetsam phase far more evenly distributed and with a mass fraction spanning a quite narrower range (0.464–0.577).

Figure 8 shows the evolution of the jetsam mass fraction profile with time obtained using the Syamlal[29] drag correlation as an example. From the figure, we note that during the first 2 s, the jetsam phase spreads rapidly throughout the system; its mass fraction is seen to gradually increase at the bottom of the bed until an even distribution is attained (fully mixed state) after about 4 s of simulation. The jetsam mixing profile varies little thereafter and therefore is not reported. In terms of the time required by the system to reach steady-state conditions, the above computational prediction is found to be at variance with experimental observations, where the bed becomes fully mixed after roughly 1 min. The difference in mixing time between experimental and computational predictions clearly reveals a limitation in the predictive capability of the model. This might be due to possible shortcomings in the closures adopted or to the fact that the stress internal to the solid phases has not been considered in the present work. The extent to which either factor predominates is presently unknown; however, it is worth pointing out that similar disparities have also been encountered by other researchers who have carried out analogous investigations while taking into account the solid stress contribution. We mention, in this regard, the work of Huilin et al.[64] where the fluid dynamic behavior of a gas-fluidized binary mixture of Geldart Group D particles is simulated starting from initial conditions of perfect mixing. In the operating conditions chosen, the system tends to segregate and within roughly 10 s almost complete segregation is predicted.

Bubble dynamics

An analysis of the bubble dynamics within the bed was carried out by comparing results in terms of computational bubble diameter with data obtained from experimental investigation. In defining a bubble, an appropriate voidage had to be selected as the boundary between emulsion and gas phases. A voidage contour of 0.80 was assumed in the simulations. This subjective figure is in conformity with values used in literature; in this regard, we refer, for instance, to the work by Yates et al.,[65] and Mazzei and Lettieri.[66] The experimental analysis of the bubble diameter was conducted using Optimas 6.0, an image analysis software. The computational analysis, on the other hand, was performed using the numerical algorithm recently developed by Mazzei and Lettieri,[66] where bubble diameters are assessed by capturing void regions within the simulated fluidized bed and then gauging their equivalent diameter (diameter of the circle of equivalent area).

Figure 9 shows a comparison between experimental and simulated bubble diameters. The data reported refer to experimental findings, results from the reference simulation where the particle–particle drag was neglected, and predictions obtained using the closure by Syamlal.[29] Results relevant to other constitutive equations have not been reported, since these did not appreciably differ from those based on the Syamlal[29] equation. Indeed, as the figure clearly shows, the theoretical predictions in terms of bubble diameter are not

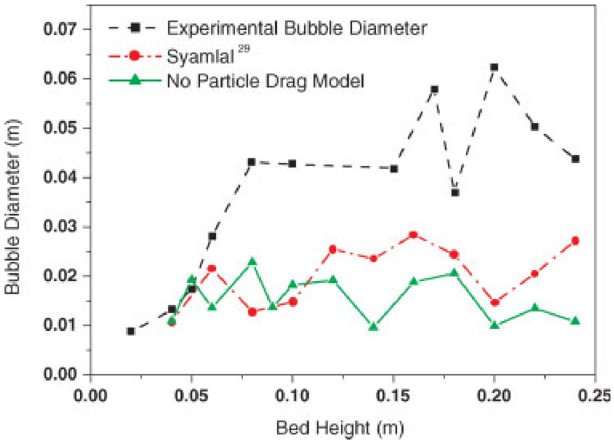

Figure 9. Comparison of experimental with the simulated bubble diameter for Syamlal[29] particle drag model and no implemented drag model.

[Color figure can be viewed in the online issue, which is available at www.interscience.wiley.com.]

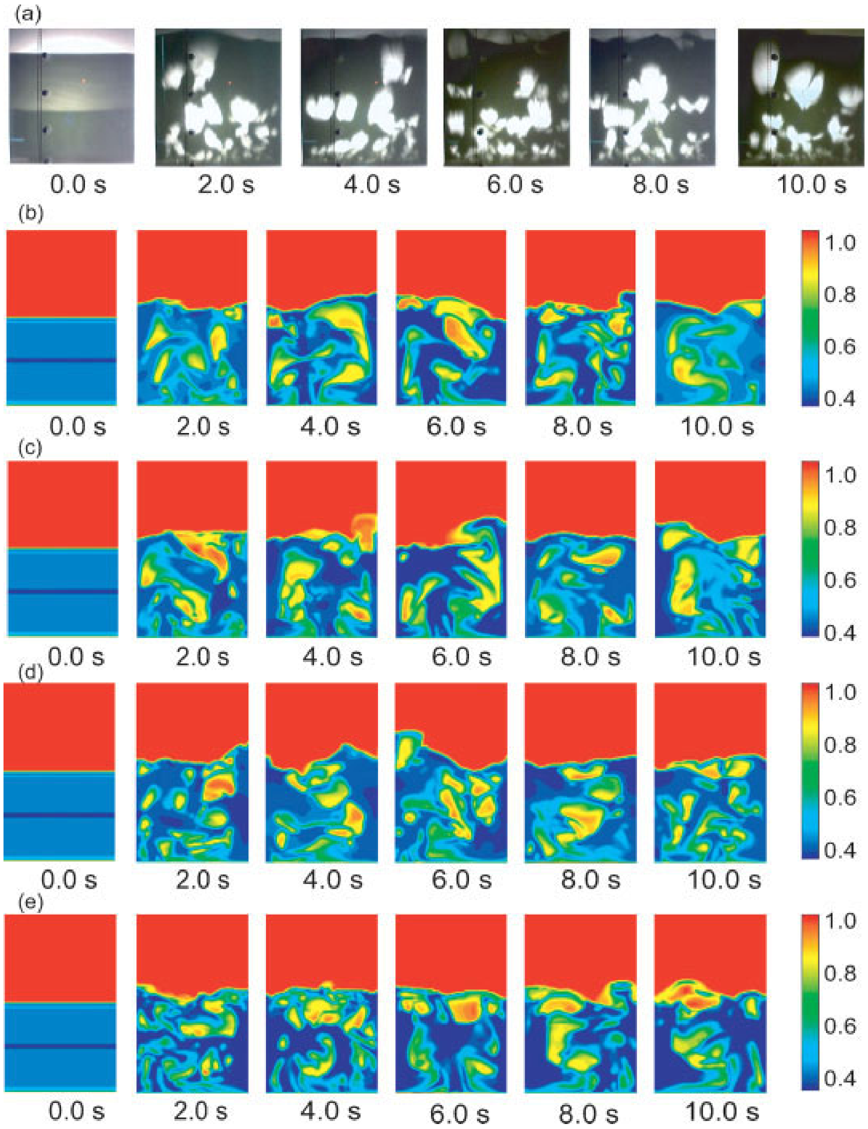

Figure 10. Snapshots showing a comparison between (a) experimental bed, (b) computational bed obtained using the drag closure by Bell,[21] (c) computational bed obtained using the drag closure by Gidaspow et al.,[20] (d) computational bed obtained using the drag closure by Syamlal,[29] and (e) computational bed obtained using no particle drag expression.

[Color figure can be viewed in the online issue, which is available at www.interscience.wiley.com.]

significantly affected by the inclusion of the particle–particle drag force; this contribution seems therefore not to have a dominant effect on the bubble dynamics of the system. The experimental bubbles are always found to be larger than the simulated ones. Experimental evidence also indicates an increase in bubble size with increasing bed height due to coalescence, a phenomenon that appears less pronounced in the numerical results. A possible cause that might contribute in the underestimation of the computed bubble size might be found in the dimensionality of the computational domain used in the simulations. A previous investigation carried out by Owoyemi et al.[9] using a 2D computational domain highlighted a disparity between experimental and predicted bubble sizes. The difference was attributed to the subtle dissimilarity in geometry between the 2D computational domain and the experimental 3D, "thin 2D," domain.

To complete the analysis, Figure 10 reports a comparison between experimental and simulated bed voidage profiles obtained using the different constitutive expressions for the particle–particle drag force previously presented. All the simulations predict the bubbling phenomenon, albeit modestly, alongside other macroscopic phenomena like bubble coalescence and bed expansion. However, once again, this specific kind of investigation does not seem to discriminate between different particle–particle drag force closures and appears to be quite insensitive to the inclusion of such term.

Bed expansion

A quantitative comparison of the bulk properties of the bed is shown in Table 5 in which results for bed height and voidage are reported. The properties were time-averaged

Table 5. Comparison of Time-Averaged Macroscopic Fluidization Properties with Experimental Data

Drag Model	Bed Height (m)	Bed Voidage
Experimental	0.365	0.520
Bell[21]	0.354	0.500
Gidaspow et al.[20]	0.353	0.498
Syamlal[29]	0.355	0.503
No particle drag implemented	0.347	0.490

ignoring the first 2 s of simulation to reduce the effect of perturbations associated with the bed start-up. Very little difference is found between the various cases examined, the percent error spanning the range 3.3% (Syamlal[29] closure)–5.8% (no particle drag implemented). Also in this instance, the computational predictions are quite insensitive to the specific particle–particle drag force closure adopted and do not seem to be significantly affected by the inclusion of such contribution. This is not entirely surprising, since the concentration profiles of the solid phases within the bed are not expected to have a marked effect on overall bed properties such as bed height and mean bed void fraction.

Effect of grid and time resolution on the simulation results

The size of the grid cells determines to a large extent the computational effort (time) required by the simulations as well as the extent of numerical diffusion. The size of the time step, on the other hand, influences the numerical convergence of the differential equations as well as the overall computational time. Thus, it is important that an optimum be found for the above quantities (cell size and time step). To this end, a study was conducted to investigate the effect of time and grid resolution on the numerical predictions of the main macroscopic fluidization properties of interest. Four simulations were carried out using uniform grids with square cells of 5 and 10 mm side length and time steps of 10E −04 and 10E −03 s. The simulation conditions employed (physical properties, initial and boundary conditions, etc.) are those reported in the *Simulations* section. Here again, the particle drag law by Syamlal[29] was used to describe the interaction between the solid phases in all the simulations.

Table 6 shows a comparison of the results in terms of averaged macroscopic fluidization properties obtained after 10 s of simulation for all the different cases considered. A change in the grid cell size is observed to have very little influence on the averaged numerical predictions of the fluidization indicators. In particular, using a constant time step of 10E −04 s and increasing the grid cell size from 5 to 10 mm results in no appreciable change in the predicted numerical values of bed height and voidage. There is a small effect on the numerical predictions of mixing index and coefficient of segregation; such an effect, however, is quite negligible within the range of variation of the two indexes (refer to *Mixing and Segregation* section under *Results and Discussion* section).

Table 6. Comparison of the Simulation Results in Terms of Averaged Fluidization Properties for the Numerical Investigation of Grid and Time Resolution

Time Step (s)	Grid Size (mm)	Bed Height (m)	Bed Voidage	Mixing Index	Coefficient of Segregation
10^{-4}	5	0.355	0.503	0.998	−0.620
10^{-3}	5	0.350	0.496	0.985	+0.951
10^{-4}	10	0.355	0.501	0.988	+0.132
10^{-3}	10	0.350	0.496	0.987	+0.211

On the other hand, a reduction in the time step from 10E −03 to 10E −04 s whilst using a constant grid cell size of 5 mm results in a 2.0% change in the numerical prediction of bed height and voidage. Here again, it appears that the effect of a time step reduction on the predictions of mixing index and coefficient of segregation is minimal. Overall, we might say that a change in time step has a slightly more pronounced effect on the numerical predictions than a corresponding change in grid cell size.

It would be desirable at this point to conduct also a study where smaller grid cells and time steps be considered; however, the long computational times involved render such a study unfeasible. With our current computational resources, simulations performed using a time step of 1.0E −04 s and square cells of 5-mm side length required an overall computational time of roughly 2200 h (92 days). For the same time step, if the side length of the cells is halved (2.5 mm), the computational time rises to about 4800 h (200 days) for the same amount of real time simulation. Similarly, for the same grid resolution, if the time step is lowered to 1.0E −05 s, the computational time rises to about 9950 h (415 days).

Effect of the solid pressure contribution on the simulation results

For completeness, the effect of the solid pressure contribution on the mixing and segregation behavior of the binary system herein examined was investigated. An additional simulation was performed with the inclusion of the isotropic part of the solid stress tensor, and without the implementation of the numerical algorithm for the solid phase compaction control developed in this work. The simple solid pressure model advanced by Bouillard et al.[67] was employed to account for the solid stress in the particulate phases. Default simulation conditions and computational parameters were used; once again, the particle drag law by Syamlal[29] was adopted to describe the interaction between the solid phases.

Table 7 reports the mixing index M and the coefficient of segregation C_s calculated from experiments and after 10 s of simulation for the two different cases. The values of M are

Table 7. Comparison of Numerical Values of Mixing Index and Coefficient of Segregation Obtained by (a) Considering and (b) Neglecting the Isotropic Contribution to the Solid Stress

Study	Solid Stress Model	Mixing Index	Coefficient of Segregation
Experimental	–	0.886	+3.520
Wu and Baeyens[10]	–	0.900	–
Default Simulation	–	0.999	−0.620
New Simulation	Bouillard et al.[67]	0.972	+1.160

Experimental results are also reported for completeness.

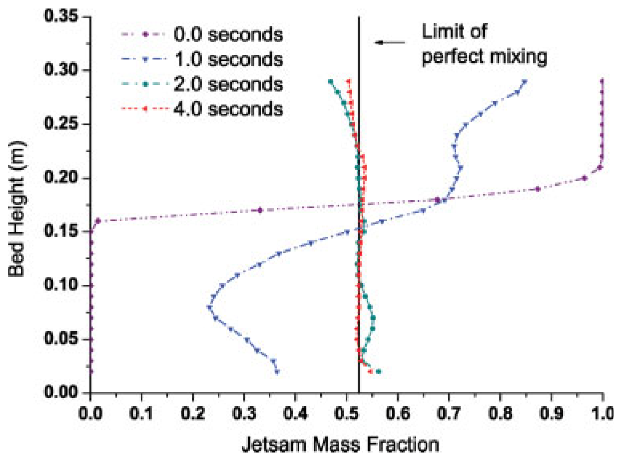

Figure 11. Evolution of the jetsam mass fraction profile with time obtained using the simple solid pressure model of Bouillard et al.[67]

[Color figure can be viewed in the online issue, which is available at www.interscience.wiley.com.]

also compared with the prediction obtained using the semi-empirical correlation by Wu and Baeyens.[19]

The two simulations, in agreement with experimental findings, yield similar results for the mixing index and coefficient of segregation. Quantitatively, as regards the mixing index, the numerical predictions that account for the isotropic solid phase stress deviate from the experimental measurements by roughly 9%; a percent error of 13% is instead found when the particle stress is neglected. Thus, it seems reasonable to conclude that the simple pressure stress considered in this study does not play a dominant role on the numerical prediction of mixing index and coefficient of segregation. Figure 11 shows the evolution of the jetsam mass fraction profile with time obtained when the isotropic solid phase stress is modeled. It can be observed that during the first 2 s, the jetsam phase spreads rapidly throughout the system in concurrence with what was shown in Figure 8, where the solid stress was neglected. In both figures, the mass fraction gradually increases at the bottom of the bed until an even distribution (fully mixed state) is finally attained after about 4 s of simulation. This seems to confirm that the computational predictions of the mixing time are not significantly affected by the inclusion of the solid pressure contribution for the solid phases.

Conclusions

This work has described the derivation of the Eulerian–Eulerian averaged equations of change for binary mixtures of solid particles fluidized by means of Newtonian fluids. The equations have been derived by applying the averaging scheme put forward by Jackson,[8,9] more specifically particle phase averages have been employed in place of the usual solid phase averages. The application of this alternative scheme, along with the various considerations presented, has added new insight into the meaning of each of the terms featuring in the equations. The origin of the particle–particle interaction force has been clearly presented; the relevance of this contribution to the fluid dynamic behavior of binary systems has been investigated and alternative closures available in literature have been examined and compared. A brief description of a new fluid dynamic model formerly developed by the authors has been given. The model has been solved using the commercial CFD code CFX 4.4. Four simulations have been carried out; three wherein different constitutive equations for the particle–particle drag force were used, and a final one where the force was entirely neglected. The first three case studies yielded similar results in terms of jetsam particle distribution within the bed, with an almost perfect mixing and a good agreement with the experimental data. In the forth case study, conversely, an overprediction of the jetsam mobility was found with a resulting tendency of such phase to segregate toward the bottom of the bed. This was in clear contrast with the experimental evidence. An investigation into the bubble dynamics and bulk properties of the system was also conducted and concluded the work. This did not discriminate between different particle–particle drag force closures and appeared to be quite insensitive to the inclusion of such a contribution. In addition, a sensitivity analysis concerning the grid and time resolution and the effect of the contribution of the solid pressure on the simulations results was carried out.

Acknowledgments

The authors wish to acknowledge financial support from the Engineering Physical Science Research Council (EPSRC), Tioxide Europe Ltd. and BP Chemicals, Hull (UK). They are also very grateful to Professor Renzo Di Felice for the stimulating discussions concerning the particle–particle drag force.

Literature Cited

1. Boemer A, Qi H, Renz U. Eulerian simulation of bubble formation at a jet in a two-dimensional fluidized bed. *Int J Multiphase Flow*. 1997;23:927–944.
2. van Wachem BGM, Schouten JC, van den Bleek CM, Krishna R. Eulerian simulations of bubbling behaviour in gas–solid fluidized beds. *Comput Chem Eng*. 1998;22:299–306.
3. Peirano E, Delloume V, Leckner B. Two- or three-dimensional simlations of turbulent gas–solid flows applied to fluidization. *Chem Eng Sci*. 2001;56:4787–4799.
4. Gelderbloom SJ, Gidaspow D, Lyczkowski RW. CFD simulations of bubbling/collapsing fluidized beds for three Geldart groups. *AIChE J*. 2003;49:844–858.
5. Lettieri P, Saccone G, Cammarata L. Predicting the transition from bubbling to slugging fluidization using computational fluid dynamics. *Chem Eng Res Des*. 2004;82:939–944.
6. Owoyemi O, Lettieri P, Place R. Experimental validation of Eulerian–Eulerian simulations of rutile industrial powders. *Ind Eng Chem Res*. 2005;44:9996–10004.
7. Anderson TB, Jackson R. A fluid mechanical description of fluidized beds. *Ind Eng Chem Fundam*. 1967;6:527–539.
8. Jackson R. Locally averaged equations of motion for a mixture of identical spherical particles and a Newtonian fluid. *Chem Eng Sci*. 1997;52:2457–2469.
9. Jackson R. Erratum. *Chem Eng Sci*. 1998;53:1955.
10. Whitaker S. The transport equations for multiphase systems. *Chem Eng Sci*. 1973;28:139–147.
11. Drew DA. Averaged field equations for two-phase media. *Stud Appl Math*. 1971;50:133–166.
12. Drew DA. Mathematical modelling of two-phase flow. *Annu Rev Fluid Mech*. 1983;15:261–291.
13. Drew DA, Lahey RT. *Analytical Modelling of Multiphase Flow. Particulate Two-Phase Flow*. London: Butterworth-Heinemann, 1993.
14. Drew DA, Segel LA. Averaged equations for two-phase flows. *Stud Appl Math*. 1971;50:205–231.

15. Nienow AW, Chessman DJ. The effect of shape on the mixing and segregation of large particles in gas-fluidized beds of small ones. In: Grace JR and Matsen JM, ed., *Fluidization*, Vol. 1. New York: Plenum, 1980:373–380.
16. Nienow AW, Rowe PN, Agbim AJ. The mechanisms by which particles segregate in gas fluidized beds—binary systems of near spherical particles. *Trans Inst Chem Eng*. 1972;50:311–319.
17. Nienow AW, Rowe PN, Chiba T. Mixing and segregation of a small proportion of large particles in gas fluidized beds of considerably smaller ones. *AIChE Sym Ser*. 1978;74:45–53.
18. Marzocchella A, Salatino P, Di Pastena V, Lirer L. Transient fluidization and segregation of binary mixtures of particles. *AIChE J*. 2000;46:2175–2182.
19. Wu SY, Baeyens J. Segregation by size difference in gas fluidized beds. *Powder Technol*. 1998;98:139–150.
20. Gidaspow D, Syamlal M, Seo Y. Hydrodynamics of fluidization of single and binary size particles: supercomputer modelling. In: *Proceedings of the Fifth Engineering Foundation Conference on Fluidization*, Vol. 5. 1985:1–8.
21. Bell RA. *Numerical Modelling of Multi-Particle Flows in Bubbling Gas–Solid Fluidized Beds*, Licentiate Thesis. Melbourne: Swinburne University of Technology, 2000.
22. Gera D, Syamlal M, O'Brien TJ. Hydrodynamics of particle segregation in fluidized beds. *Int J Multiphase Flow*. 2004;30:419–428.
23. Cooper S, Coronella CJ. CFD simulations of particle mixing in a binary fluidized bed. *Powder Technol*. 2005;151:27–36.
24. van Wachem BGM, Schouten JC, van den Bleek CM, Krishna R, Sinclair JL. CFD modeling of gas-fluidized beds with a bimodal particle mixture. *AIChE J*. 2001;6:1292–1302.
25. Soo SL. *Fluid Dynamics of Multiphase Systems*. Waltham: Blaisdell Publishing, 1967.
26. Nakamura K, Capes CE. Vertical pneumatic conveying of binary particle mixtures. In: Keairns, D, ed. *Fluidization Technology*, Vol. 2. Washington, DC: Hemisphere Publishing. 1976:159–184.
27. Arastoopour H, Wang CH, Weil SA. Particle–particle interaction force in a dilute gas–solid system. *Chem Eng Sci*. 1982;37:1379–1384.
28. Srinivasan MG, Doss ED. Momentum transfer due to particle-particle interaction in dilute gas–solid flows. *Chem Eng Sci*. 1985;40:1791–1792.
29. Syamlal M. *The Particle–Particle Drag Term in a Multiparticle Model of Fludization*, Topical Report. Springfield: National Technical Information Service, 1987.
30. Wallis GB. *One Dimensional Two-Phase Flow*. New York: McGraw-Hill, 1969.
31. Gidaspow D. *Multiphase Flow and Fluidization*. London: Academic Press, 1994.
32. Jackson R. *The Dynamics of Fluidized Particles. Cambridge Monographs on Mechanics*. Cambridge: Cambridge University Press, 2000.
33. Maxey MR, Riley JJ. Equation of motion for a small rigid sphere in a nonuniform flow. *Phys Fluids*. 1983;26:883–889.
34. Nadim A, Stone HA. The motion of small particles and droplets in quadratic flows. *Stud Appl Math*. 1991;85:53–73.
35. Zhang DZ, Prosperetti A. Averaged equations for inviscid disperse two-phase flow. *J Fluid Mech*. 1994;267:185–219.
36. Zhang DZ, Prosperetti A. Momentum and energy equations for disperse two-phase flows and their closure for dilute suspensions. *Int J Multiphase Flow*. 1997;23:425–453.
37. Saffman PG. The lift on a small sphere in a slow shear flow. *J Fluid Mech*. 1965;22:385–400.
38. Auton TR, Hunt JCR, Prud'homme M. The force exerted on a body in inviscid, unsteady, non-uniform, rotational flow. *J Fluid Mech*. 1988;197:241–257.
39. Ding J, Gidaspow D. A bubbling fluidization model using kinetic theory of granular flow. *AIChE J*. 1990;36:4.
40. Gelderbloom SJ, Gidaspow D, Lyczkowski RW. CFD simulations of bubbling/collapsing fluidized beds for three Geldart groups. *AIChE J*. 2003;49:4.
41. Massoudi M, Rajagopal KR, Ekmann JM, Mathur MP. Remarks on the modeling of fluidized systems. *AIChE J*. 1992;38:3.
42. van Wachem BGM, Schouten JC, van den Bleek CM, Krishna R, Sinclair JL. Comparative analysis of CFD models of dense gas–solid systems. *AIChE J*. 2001;5:1035–1051.
43. Owoyemi O. CFD *Modelling of Binary Gas Fluidized Beds*, MPhil Thesis. London: University College London, 2005.
44. Owoyemi O, Lettieri P. A hydrodynamic model for the simulation of binary particle systems in gas-fluidized beds. In: *Proceedings of the 10th International Conference on Multiphase Flow in Industrial Plant*, Vol. 1. 2006:459–470.
45. Di Felice R. Liquid Fluidization of Binary Solid Mixtures, Licentiate Thesis. London: University College London, 1988.
46. Foscolo PU, Gibilaro L. Fluid dynamic stability of fluidized suspensions: the particle bed model. *Chem Eng Sci*. 1987;42:1489–1500.
47. Gibilaro L. *Fluidization Dynamics*. London: Butterworth Heinemann, 2001.
48. Mazzei L, Lettieri P, Elson T, Colman D. A revised mono-dimensional particle bed model for fluidized beds. *Chem Eng Sci*. 2006;61:1958–1972.
49. Lebowitz JL. Exact solution of generalised Percus-Yevick equation for a mixture of hard spheres. *Phys Rev*. 1964;133:895–899.
50. Lettieri P, Cammarata L, Micale G, Yates J. CFD simulations of gas fluidized beds using alternative Eulerian–Eulerian modelling approaches. *Int J Chem Reactor Eng*. 2003;1:1–21.
51. Fedors RF, Landel RF. An empirical method of estimating the void fraction in mixtures of uniform particles of different sizes. *Powder Technol*. 1979;23:225–231.
52. Guenther C, Syamlal M. The effect of numerical diffusion on the simulation of isolated bubbles in gas–solid fluidized beds. *Powder Technol*. 2001;116:142–154.
53. Lettieri P, Micale G, Cammarata L, Colman D. Computational fluid-dynamics simulations of gas fluidized beds: comparison of different modelling approaches. In: *Proceedings of the 10th Workshop of Two-phase Flow Predictions*, Vol. 1, Merseburg, Germany. 2002: 300–309.
54. Samuelsberg A, Hjertager BH. Computational modeling of gas/particle flow in a riser. *AIChE J*. 1996;42:1536–1546.
55. Enwald H, Almstedt AE. Fluid dynamics of a pressurized fluidized bed: comparison between numerical solutions from two-fluid models and experimental results. *Chem Eng Sci*. 1999;54:329–342.
56. van Wachem BGM. *Derivation, Implementation and Validation of Computer Simulation Models for Gas–Solid Fluidized Beds*, Licentiate Thesis. Amsterdam: Delft University, 2000.
57. Mathiesen V, Solberg T, Hjertager BH. Predictions of gas/particle flow with an Eulerian model including a realistic particle size distribution. *Powder Technol*. 2000;112:34–45.
58. McKeen T, Pugsley T. Simulation and experimental validation of a freely bubbling bed of FCC catalyst. *Powder Technol*. 2003;129: 139–152.
59. Toomey RD, Johnstone HF. Gaseous fluidization of solid particles. *Chem Eng Prog*. 1952;48:220–226.
60. Davidson JF, Harrison D. *Fluidised Particles*. Cambridge: Cambridge University Press, 1963.
61. Gossens WRA, Dumont GL, Spaepen GL. Fluidization of binary mixtures in the laminar flow region. *Chem Eng Prog Symp Ser*. 1971;67:38–45.
62. Rowe PN, Nienow AW, Agbim AJ. A preliminary quantitative study of particle segregation in gas fluidized beds—binary systems of near spherical particles. *Trans Inst Chem Eng*. 1972;50:324–333.
63. Geldart D. Gas Fluidization Technology. London: Wiley, 1973.
64. Huilin L, Yurong H, Gidaspow D. Hydrodynamic modelling of binary mixture in a gas bubbling fluidized bed using the kinetic theory of granular flow. *Chem Eng Sci*. 2003;58:1197–1205.
65. Yates JG, Cheesman D, Sergeev YA. Experimental observations of voidage distribution around bubbles in a fluidized bed. *Chem Eng Sci*. 1994;49:1885–1895.
66. Mazzei L, Lettieri P. A numerical algorithm for the analysis of the bubble dynamics in 2D fluidized beds simulated by means of CFD multiphase codes. *Int J Chem Reactor Eng*. 2006;4:1–20.
67. Bouillard JX, Lyczkowski RW, Gidaspow D. Porosity distributions in a fluidized bed with an immersed obstacle. *AIChE J*. 1989;35: 908–922.

Manuscript received Nov. 14, 2006, and revision received May 8, 2007.